A Data-Based Derivation of the Internal Stress in the Discrete-Continuum Transition Regime of Dislocation Based Plasticity

Sing-Huei Lee[a,b], Katrin Schulz[a,b,*]

[a]Karlsruhe Institute of Technology (KIT), Institute for Applied Materials (IAM), Karlsruhe, Germany
[b]Karlsruhe University of Applied Sciences (HKA), Karlsruhe, Germany

ARTICLE INFO

Keywords:
Dislocations
Continuum crystal plasticity
Homogenization
Material length scale
Grain boundaries
Discrete-continuous transition

ABSTRACT

Effectively homogenizing microstructure heterogeneity within the coarse-graining volume is a long-lasting challenge in crystal plasticity theories. In this paper, we propose a data-based homogenization method that utilizes discrete dislocation dynamic simulations to derive the nearfield correction stress (back stress) for continuum models. This stress accounts for the effective stress field induced by microstructure heterogeneity under the length scale of a coarse-graining volume, providing a physically based homogenization approach. To bridge the gap between discrete and continuous regimes, we introduce two versions of the nearfield correction stress, as well as a criterion based on microstructure and numerical parameters to determine the discrete and continuous transition. Moreover, by analyzing the mathematical connections with the work-conjugated gradient plasticity theory, we further provide a physical explanation for the observed material length scale in the thermodynamically consistent back stress term. This work presents a novel methodology for effectively addressing microstructure heterogeneity and advancing the understanding and modeling of material behavior bridging different length scales.

1. Introduction

The motion and interaction of dislocations are fundamental for understanding and predicting the mechanical behavior of materials. Continuous crystal plasticity has made significant advancements in recent years by incorporating microstructural mechanisms into modeling approaches. Notably, studies conducted, e.g., by Yefimov et al. (2004); Gurtin et al. (2007); Gurtin and Ohno (2011); Hochrainer et al. (2014); Geers et al. (2014); Cui et al. (2015); Sudmanns et al. (2019); Ryś et al. (2020); Lin and El-Azab (2020); Vivekanandan et al. (2023) have contributed to this field by integrating mechanism-based knowledge into continuum modeling frameworks. In these models, microstructural information is represented by state variables such as dislocation density, stress, dislocation flux, and dislocation velocity within the elements, achieved through a homogenization strategy. By considering microstructural effects in a continuous manner, continuum models offer computational efficiency compared to discrete models while still capturing the advantages of incorporating microstructural characteristics.

Within the continuum models, there have been plenty of references showing the use of crystal plasticity capturing non-uniform deformation induced by the existence of multiple grains, precipitations, and gradient of mechanical properties, e.g., Ma et al. (2006), Roters et al. (2010), Izadbakhsh et al. (2011), Jafari et al. (2017), Bhattacharyya et al. (2019), Li et al. (2022). Within these theories, homogenization approaches have been proposed to address the non-uniform structure at the length scale of several microns, even across grains. However, Berdichevsky and Dimiduk (2005); Roy et al. (2008) have pointed out that the applicability of continuum theories is doubtful as the discretization level shrinks to the scale close to dislocation spacing. Addressing microstructure heterogeneity within the coarse-graining volume under such a smaller scale remains one of the challenges for continuum theories. Here, the heterogeneity of the scale close to dislocation spacing refers to the inhomogeneous microstructural features, such as dislocation patterning and pile-up, occurring at the length scales smaller than the numerical resolution employed in continuous simulations. It usually occurs in the region with highly non-uniform deformation, e.g. in the proximity of grain boundaries and inclusions, or regions with high strain gradient. Therefore, the coarse-graining volume under such conditions should take the heterogeneities into account. Another challenge of continuum modeling is the derivation of physical-based homogenization strategies. The models usually include many parameters that have to be taken into

*Corresponding author: katrin.schulz@kit.edu (Katrin Schulz)

the constitutive formulation. Mostly, these parameters are very difficult or even impossible to be measured from experiments and have to be approximated, e.g. based on theoretical considerations of possible ranges. The direct homogenization from discrete to continuum formulation without unknown or non-physical input parameters is still missing within the field of continuum theories.

To bridge the gap between discrete and continuum theories by considering the heterogeneity, smaller scales of homogenization approaches have been proposed. For instance, Geers et al. (2013) have considered a system of parallel straight edge dislocations, and further derived the effective stress field induced by dislocation pile-up as a back stress term. In continuous dislocation dynamic theory (CDD), an internal correction stress having the role of back stress within the flow rule has been introduced. This correction stress considers the heterogeneity effect induced by the short-range interactions between excessive dislocations within the coarse-graining volume. It was motivated by the back stress proposed within the statistical theory by Groma et al. (2003, 2007); Ispánovity et al. (2008); Groma et al. (2016). And a further extension to numerical modeling proposed by Schulz et al. (2014); Schmitt et al. (2015) mitigates errors caused by different sizes of coarse-graining. Meanwhile, Dogge et al. (2015) has started from a more idealized dislocation configuration (e.g., the Taylor lattice) and derived the correction effect induced by the heterogeneity considering both the excessive and total dislocations. In these derivations, the correction stress (back stress) has formulations scaled by the inverse of the square root of the dislocation density homogenized within the coarse-graining. A similar scaling characteristic is also commonly applied in the back stress conjugated with the energetic defect energy potential within gradient plasticity theory. This scaling is more often denoted as the square of material length scale (e.g., Gurtin (2000)). Berdichevsky (2006) has introduced a "saturation density of the crystal" as a scaling for the non-convex logarithmic energy potential. Constant values of saturation densities are further obtained for Al and Ni. This finding bridges the material length scale derived from thermodynamic consistency toward microstructure mechanisms. However, the discussions by Norfleet et al. (2008); Zaiser (2015); Hochrainer (2016); Forest (2019); Piao and Le (2022) show the uncertainty of dwelling upon the question of the correct definition for the scaling density. Up to now, there is still no physical-based explanation for the role of "saturation density" from microstructure point of view. Also, the magnitude of the scaling density still remains an open issue for numerical implementations (e.g., Wulfinghoff and Böhlke (2015); Ryś and Petryk (2018); Albiez et al. (2019); Jebahi et al. (2020)). It has been concluded by Voyiadjis and Song (2019) that the precise definition and magnitude for both the defect energy potential as well as the material length scale are still controversial.

Hence, based on the presumption that the presence of the correction stress within the continuous flow rule emerges due to the heterogeneity in coarse-graining volume, we propose a data-based homogenization strategy addressing the microstructure heterogeneity and the derivation for the correction stress (back stress). Considering a bottom-up methodology (i.e., transitioning from the discrete to continuous scale), we derive a back stress formulation as well as reveal a deeper understanding of the physical aspects governing the homogenized stress field in the framework of crystal plasticity theories. The derivation procedure encompasses several key aspects:

- Identifying microstructure heterogeneity.
- Representative dislocation configurations in the discrete-to-continuum regime.
- Homogenization strategy for capturing internal length scales.

Within Section 2, we construct a discrete dislocation dynamic (DDD) benchmark simulation to gain insights into the formation and characteristics of microstructure heterogeneity within a coarse-graining volume. Based on the results of DDD benchmark simulations from Section 2, we derive representative microstructure configuration for an averaging volume of continuum theories in Section 3. The configuration takes the formation of inhomogeneously distributed edge dislocation walls within the coarse-graining into account. We further propose a homogenization strategy by introducing the effective stress addressing the heterogeneity within the coarse-graining. To determine the heterogeneous distribution within the coarse-graining induced by different microstructure and numerical conditions, we adopt a data-based approach to determine the probability distribution of edge dislocation walls within Section 4. Within Section 5, we derive a formulation for the effective internal stress induced by microstructural heterogeneity. The direct homogenization from discrete to continuum formulation as presented in this study physically addresses microstructure heterogeneity within the coarse-graining. At the same time, we avoid unknown input parameters for the continuum model. The homogenization strategy is then a purely physical outcome of a continuum formulation that is able to represent the internal stress fields. It is important to distinguish between the applicable domain of homogenization for the effective internal stress fields and the whole system domain. Within this study, we aim to

investigate the microstructure features under the length scale of a coarse-graining volume, which contains highly heterogeneous dislocation distributions. It has to be remarked that this addresses the heterogeneity in every single averaging element which is in most cases different from the microstructure heterogeneity distributed throughout the whole system. The derivation comes along with a criterion for identifying the transition regime between continuous and discrete modeling approaches. This nearfield correction stress is derived for a highly flexible numerical discretization scheme based on both the microstructure and numerical length scales of the coarse-graining volume. Moreover, the presented results yield insights into a longstanding problem: the physical explanation of the material length scale within work-conjugated gradient plasticity.

2. Discrete Analysis of Heterogeneity in Continuous Crystal Plasticity Coarse-graining

In this section, we explore the heterogeneity formation within a coarse-graining volume by discrete-level simulation. We introduce a benchmark DDD simulation setup that calculates dislocation mobility within spatial coarse-graining under the influence of adjacent elements. Thereby, the emergence of microstructural heterogeneity formation at length scales smaller than the numerical resolution can be revealed.

2.1. Benchmark System by Discrete Dislocation Dynamic Simulation

The use of continuous crystal plasticity theory in representing dislocation arrangements within an element employs state variables, such as dislocation density. However, this approach fails to explicitly consider the microstructure heterogeneity within a coarse-graining volume. We therefore investigate the microstructure heterogeneity in a coarse-graining volume as a first step. To achieve this goal, a 2D DDD simulation, which simulates the microstructure evolution within an element, is constructed. This approach builds on the pioneering works of Amodeo and Ghoniem (1990); Van der Giessen and Needleman (1995); Groma et al. (2003).

The reason for using DDD simulations arises from the pronounced nature of microstructure heterogeneity under non-uniform deformation conditions, such as bending, indentation, or deformation in the proximity of obstacles or grain boundaries. At low temperatures, edge dislocations represent the primary mode of deformation, with out-of-plane movements such as dislocation climb and cross-slip being negligible in a simplifying assumption. As a result, the short-range interaction caused by the same slip system becomes crucial within a small range, such as a coarse-graining volume, during low-temperature non-uniform deformation. Although the 2D DDD simulation overlooks 3D mechanisms such as junction formation and inter-slip system interactions, it is still an effective tool for identifying short-range dislocation interactions within a single slip system, as demonstrated by numerous studies in the literature (Kuykendall and Cai (2013); Keralavarma and Curtin (2016)). Additionally, as mentioned in Gurtin and Ohno (2011), the interaction between slip systems is supposed to become important at length scales above a few microns, which is larger than the length scale of a single element. Therefore, the 2D DDD simulation can be utilized to observe the microstructure heterogeneity induced by the short-range effect of dislocations belonging to the same slip system within a single coarse-graining volume. Consequently, this study commences with a 2D DDD simulation that solely considers edge dislocation and a single slip system.

Fig. 1 demonstrates the geometry of the three-element coarse-graining DDD simulation we consider for investigating the microstructure heterogeneity within an element. Here, x-direction is the slip direction, and y-direction is the normal of slip plane. The edge dislocations in the DDD simulation are only capable of gliding along the slip direction and do not exhibit any out-of-plane movement. The velocity v_i of an individual dislocation i with sign s_i is determined solely by the Peach-Koehler force exerted by all neighboring dislocations j, in the absence of external loading. It is commonly assumed that the dislocation velocity is isotropic and over-damped for DDD simulation in the literature (Groma et al. (2003, 2016)). Therefore, the velocity of each dislocation is proportional to the resulting shear stress, given by

$$v_i = \frac{|\boldsymbol{b}|}{\boldsymbol{B}} s_i \tau_{\mathrm{r}}, \tag{1}$$

where $|\boldsymbol{b}|$ is the magnitude of the Burgers vector of the dislocation, $\boldsymbol{B}$ is the drag coefficient, and τ_{r} is the resolved shear stress induced by all other dislocations j, given by

$$\tau_{\mathrm{r}} = \sum_{j \neq i}^{N} s_j \frac{\mu\,|\boldsymbol{b}|}{(1-\nu)2\pi} \frac{\tilde{x}(\tilde{x}^2 - \tilde{y}^2)}{(\tilde{x}^2 + \tilde{y}^2)^2}, \tag{2}$$

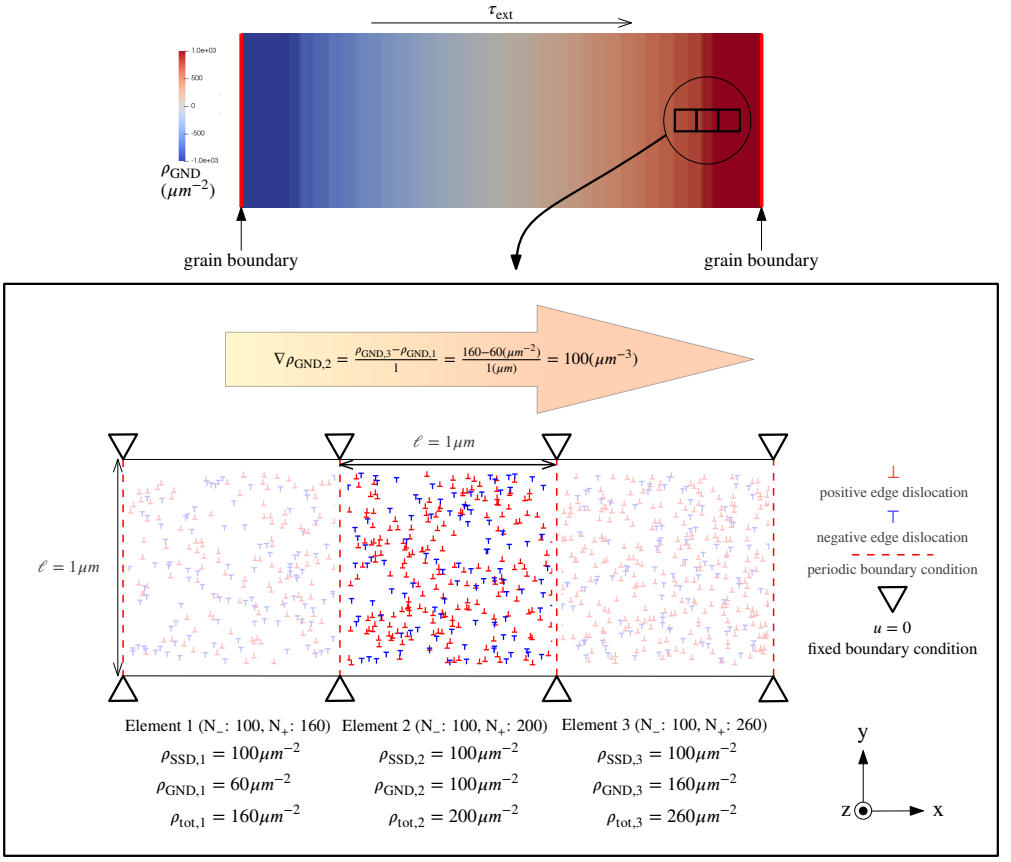

Figure 1: The geometry arrangement and setup for the three-element coarse-graining DDD simulation.

where μ is the shear modulus, ν is the Poisson's ratio, and N is the total number of dislocations. The distance between dislocation j and the target dislocation i is denoted as $\tilde{x} = x_j - x_i$ and $\tilde{y} = y_j - y_i$.

In order to analyze microstructure heterogeneity influenced by coarse-graining using the DDD method, a three-element benchmark system is introduced. The system takes into account the influence of adjacent elements (Element 1 and 3) on the targeted element (Element 2). The motion of edge dislocations within the targeted element is affected not only by the dislocations within its own element but also by all the dislocations within the adjacent elements. Within each element, random initial seeding of edge dislocations is performed.

We use the three-element setup to investigate a localized domain under high strain gradient, e.g., the GND pile up in the proximity of grain boundaries as shown in Fig. 1. Without loss of generality, the positive dislocations are assumed to be excessive. To be noted, we construct the three-element DDD simulation to investigate the microstructure distribution within a localized high strain gradient domain, instead of a whole system. The non-zero long-range average stress induced by the excessive dislocations has been addressed by the fixed boundary condition on the boundaries of the elements. This setup is similar to that: In a numerical continuum problem, the existence of non-zero net GND within the coarse-graining will cause the long-range average stress and therefore geometry incompatibility on the boundaries of elements. This issue is addressed in the numerical solution by the introduction of the mean-field stress while resolving the eigenstrain problem, which has been discussed within Lemarchand et al. (2001); Sandfeld et al. (2013); Hochrainer et al. (2014); Schulz et al. (2014). Within this study, we are not using the three-element simulation to resolve a real mean field problem for an overall domain. In contrast, we are studying a localized domain and focusing on identifying the cause of the internal stress within one single element. Therefore, the domain of the three-element simulation does not represent an overall system, but a localized domain with excessive dislocations. According to the number of positive and negative dislocations, N_+ and N_-, respectively, the corresponding state variables, such as dislocation density and gradient of dislocation density, for continuum models can be calculated. Dislocation densities, such as SSDs and

GNDs, are commonly used to describe the microstructure status in dislocation-based crystal plasticity theories. Based on the geometrical differences between GNDs and SSDs, dipole and multipole structures form when SSDs are present, while excessive dislocations are considered as GNDs (Arsenlis and Parks (1999)). The edge dislocations within the coarse-graining volume are assumed to be straight "dislocation lines" along the z-direction of Fig. 1. Within this study, we assume all the non-excessive (i.e., negative) dislocations will form into a dipole or multiple structures in a converged state. The number of non-excessive dislocations will correspond to the number of SSDs. Therefore, the SSD density can be expressed as:

$$\rho_{\mathrm{SSD}} = \frac{\mathrm{N\_} \times \ell}{\ell^3} = \frac{\mathrm{N\_}}{\ell^2}. \tag{3}$$

The number of excessive dislocations (i.e., positive dislocations deduct negative dislocations) will correspond to the number of GNDs, given by

$$\rho_{\mathrm{GND}} = \frac{\left(\mathrm{N}_+ - \mathrm{N\_}\right) \times \ell}{\ell^3} = \frac{\left(\mathrm{N}_+ - \mathrm{N\_}\right)}{\ell^2}. \tag{4}$$

And the total dislocation density, ρ_{tot}, is the summation of ρ_{GND} and ρ_{SSD}. For the state variable representing the influence of the adjacent elements, the gradient of dislocation densities is calculated as $\nabla\rho_2 = \frac{\rho_3 - \rho_1}{\ell}$, where $\nabla\rho_2$ is the gradient of dislocation density across Element 2, and ρ_n denotes the specific dislocation density within element n and ρ can be replaced by different types (i.e., SSD, GND, or total dislocation density) of dislocation density.

If we assume that the deformation during each simulation time step in continuum simulations is quasi-static, the microstructure within each simulation time step should reach an equilibrium state before moving on to the calculation for the next time step. Therefore, to simulate the microstructure evolution for a coarse-graining volume, the corresponding state variables within each averaging element are considered to be constant. To ensure the constancy of the state variables within each element throughout the DDD benchmark, a periodic boundary condition is implemented, as indicated by the red dashed lines in Fig. 1. The boundary condition is similar to a simple periodic boundary condition allowing dislocations leaving and re-entering the coarse-graining. However, the dislocations are not allowed to transmit through adjacent elements. In other words, each element (domain) contains dislocations interacting with dislocations in the other element (domain), but the dislocations within each domain do not transfer. Thereby, we ensure to maintain constant state variables (e.g. dislocation density and gradient) within each coarse-graining volume, and the final microstructure is achieved under a quasi-static condition obtained with constant state variables.

2.2. The Heterogeneity Formation within a Coarse-graining Volume

To identify the heterogeneity forming within a coarse-graining volume, we analyze the benchmark system demonstrated in Section 2.1 calculating the microstructure of copper materials. The material properties used for the simulation are as follows: the shear modulus μ is set to 40.0 GPa and the Poisson's ratio ν is set to 0.367, as reported in Date and Andrews (1969). The length of the Burgers vector $|b|$, is determined to be 0.254 nm based on Davey (1925). Additionally, the value of $\boldsymbol{B}$ is chosen as 5×10^{-5} sPa according to Kubin et al. (1992), representing the drag coefficient for dislocation motion for the under-damped assumption.

Fig. 2a illustrates the relaxed microstructure within the targeted element (Element 2), resulting from the setup shown in Fig. 1. The resulting microstructure heterogeneity includes the presence of dipoles and multipoles formed by dislocation interaction, as shown in Fig. 2b, and edge dislocation walls consisting of excessively positive dislocations, as shown in Fig. 2c. The dipoles and multipoles are randomly positioned, while the edge dislocation walls exhibit a non-uniform distribution along the x-direction within the coarse-graining element. Based on the definition within Arsenlis and Parks (1999), we conclude the heterogeneities forming within the coarse-graining volume include the randomly seeding SSDs, as well as the non-uniformly distributed GND walls.

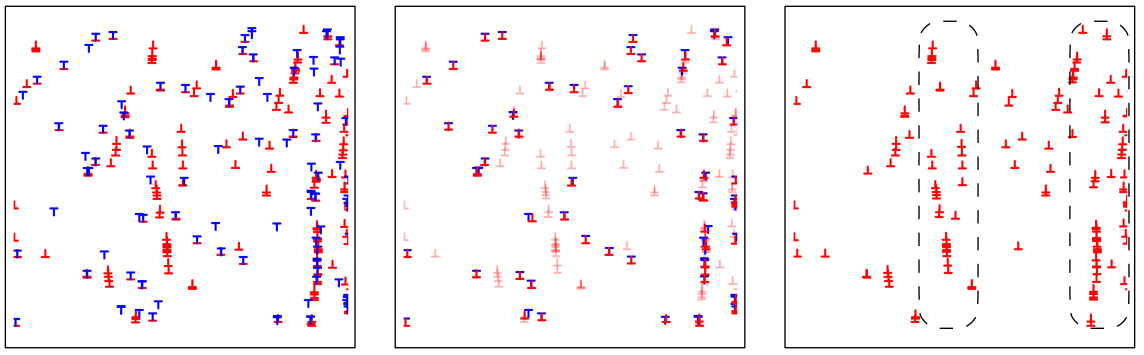

(a) (b) (c)

Figure 2: Identifying heterogeneous structure within Element 2 by the benchmarked DDD simulation. The postprocessed images are shown in (a): relaxing status to simulate a quasi-static time step; (b): dislocation dipoles and multiples; (c): the edge dislocation wall structure (highlighted by the black dashed box) is found.

3. Homogenization for Continuum Crystal Plasticity Theories

In this section, we present an extended analysis focusing on the homogenization strategy for the coarse-graining volume building upon the findings in Section 2.2. We first demonstrate the impact of heterogeneous structures based on randomly positioned SSDs and GND walls by visualizing the associated stress fields. To account for the heterogeneity within the coarse-graining, we further quantify the resulting internal stress field as a homogenization approach.

3.1. Impacts of Dislocation Configuration within a Coarse-graining

As elaborated in Section 2, the microstructure comprises randomly distributed dipoles and multipoles, along with edge dislocation walls formed by excessively positive dislocations, as depicted in Fig. 2b and Fig. 2c, respectively. Here, we investigate the impacts of the two heterogeneities by visualizing the stress fields induced by different heterogeneous structures within Element 2, we divide the element into a grid of 100×100 cells. By calculating the cumulative shear stress at the centroid of each cell, caused by all dislocations within the element, we can quantify the internal stress field within the coarse-graining. The stress fields induced by these microstructural features are presented in Fig. 3, where Fig. 3a demonstrates the stress field induced by the randomly distributed SSDs, and Fig. 3b showcases the stress field induced by the non-uniformly distributed GND walls. For a better comparison, Fig. 3c is the same as Fig. 3a, but we tune the scale bar the same as Fig. 3b, and also remove the mark of positive and negative dislocations. The results reveal that the stress field induced by dipoles and multipoles is short-range, exhibiting rapid decay to zero within a small distance and yielding an overall stress-free region within the coarse-graining (1.5 MPa in average). In contrast, the stress field induced by the GND walls is predominantly negative given the considered slip direction, exhibiting a significant magnitude (468 MPa in average) throughout the coarse-graining volume. To be noted, from Fig. 3c, within the close region of each dipole and multiple, the stress induced by each SSD still exhibits a noticeable value of stress.

Based on the findings presented in Fig. 3, we conclude that the influence arising from dipoles and multiples (SSDs) is rather low and can be neglected in the continuous configuration. However, it is crucial to consider the stress induced by excessive dislocation walls (GND walls). Taking the observed heterogeneity into account, we have to consider a certain homogenized configuration of GND walls in a coarse-graining volume. A schematic sketch of the proposed configuration within this study is given by Fig. 4. The excessive dislocations form GND walls, which are highlighted by the dashed box. Within each GND wall, the dislocations are assumed to be equally spaced with a distance L for simplicity. L are approximated by the average spacing between excessive dislocations, therefore, $L \approx \frac{1}{\sqrt{\rho_{GND}}}$. Consequently, the total number of slip planes within a coarse-graining element along the y-direction is given by $N_y = \ell \sqrt{\rho_{GND}}$. The walls are distributed non-uniformly along the x-direction, resulting in a noticeable non-zero net stress field within the coarse-graining.

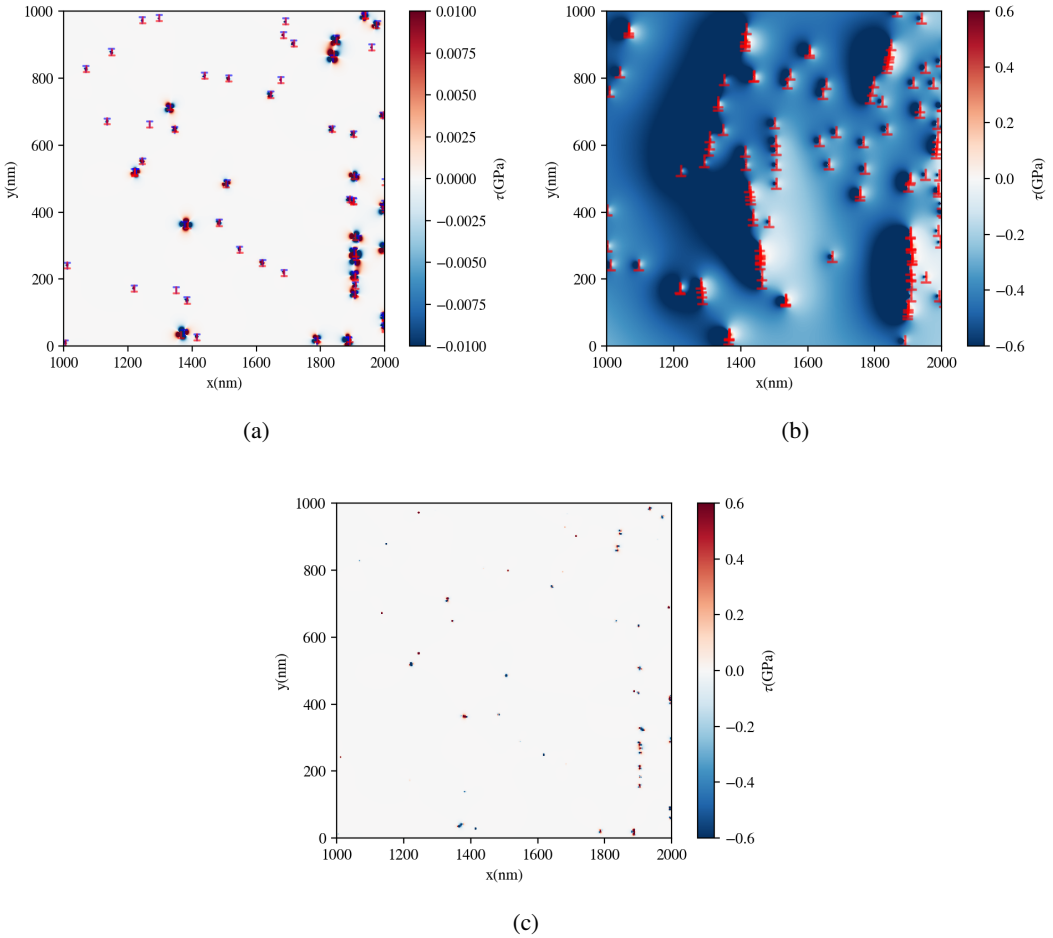

Figure 3: Illustration of the stress fields induced by different heterogeneous microstructures in a coarse-graining (Element 2). (a) shows the stress field induced by dipoles and multipoles, while (b) shows the stress field induced by GND walls. The colors represent the magnitude and sign of the stress field, with red indicating positive stress, white indicating zero stress, and blue indicating negative stress. For better comparison, (c) is the stress field induced by dipoles and multipoles but with the same scaling bar as (b).

3.2. Effective Correction Stress for Heterogeneous microstructure

To address the effect induced by microstructure heterogeneity within the coarse-graining as shown in Fig. 4, we define the effective internal stress (nearfield correction stress), $\tau^{\xi}_{\mathrm{nfc}}$. $\tau^{\xi}_{\mathrm{nfc}}$ is formulated to account for the stress field induced by the non-uniformly distributed GND walls within the coarse-graining volume on slip system ξ. To be noted, the heterogeneity effect we are addressing within this study is induced within a coarse-graining volume. Therefore, the interaction considered here forming the heterogeneity features is limited to at least one or two orders smaller than the overall simulated system, depending on the discretization level. As mentioned in Gurtin and Ohno (2011), the interaction between slip systems becomes important at length scales above a few microns. We assume that $\tau^{\xi}_{\mathrm{nfc}}$ does not involve the forest densities hardening and hence the interaction between different slip systems.

Considering the generalized Orowan's equation, which describes the relation between the plastic slip rate, $\dot{\gamma}^{\xi}$, mobile dislocation density, ρ^{ξ}_{m}, and the average dislocation velocity v^{ξ} on slip system ξ, is given by

$$\dot{\gamma}^{\xi} = |\boldsymbol{b}|\, \rho^{\xi}_{m} v^{\xi}. \tag{5}$$

While the coarse-graining volumes are under non-uniform deformations, the resulting stress can be calculated by resolving the eigenstrain problem discussed by Lemarchand et al. (2001); Sandfeld et al. (2013); Hochrainer et al. (2014); Schulz et al. (2014). The resulting shear stress on slip system ξ is the projection of the stress onto the slip

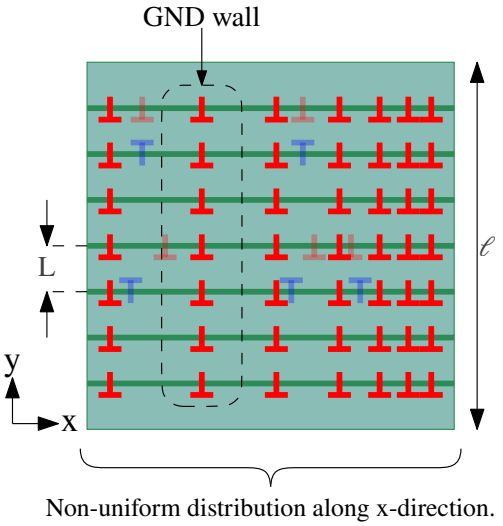

Figure 4: Spatial distribution of excessive dislocations within a coarse-graining element in continuous crystal plasticity theory.

system ξ by Schmid's factor and denoted as τ^{ξ}. We further consider the heterogeneous effect within the coarse-graining as discussed within Section 2, the resulting shear stress becomes $\tau^{\xi} - \tau^{\xi}_{\mathrm{nfc}}$. Similar to Eq. (1), v^{ξ} can be approximated by

$$v^{\xi} = \frac{|\boldsymbol{b}|}{B} \mathrm{sgn}\left(\tau^{\xi} - \tau^{\xi}_{\mathrm{nfc}}\right) \left[\left|\tau^{\xi} - \tau^{\xi}_{\mathrm{nfc}}\right| - \tau^{\xi}_{\mathrm{y}}\right], \tag{6}$$

if the resulting shear stress exceeds the yield stress τ^{ξ}_{y}. Here, τ^{ξ}_{y} induces the hindering effect resulting from forest dislocation densities from different slip systems. Thus, we obtain

$$\dot{\gamma}^{\xi} = \frac{|\boldsymbol{b}|^2 \rho^{\xi}_{m}}{B} \mathrm{sgn}\left(\tau^{\xi} - \tau^{\xi}_{\mathrm{nfc}}\right) \left[\left|\tau^{\xi} - \tau^{\xi}_{\mathrm{nfc}}\right| - \tau^{\xi}_{\mathrm{y}}\right]. \tag{7}$$

This motivates the evolution of plastic slip for dislocation-based crystal plasticity (c.f., Yefimov et al. (2004); Hochrainer et al. (2014); Schulz et al. (2019)), and in general share the same form with the simplified visco-plasticity power law model as the power equal to one (c.f., Evers et al. (2002); Geers et al. (2006); Gurtin and Ohno (2011)). The role of $\tau^{\xi}_{\mathrm{nfc}}$ within the flow rule Eq. (7) is a back stress term contributing to kinematic hardening.

The stress $\tau^{\xi}_{\mathrm{nfc}}$ can be defined as the convolution between the GND wall density $\kappa_{\mathrm{GNDwall}}(\mathrm{r})$ and the stress field induced by a single GND wall $\tau_{\mathrm{wall}}(\mathrm{r})$, given by

$$\tau^{\xi}_{\mathrm{nfc}} = \int_{\Omega} \kappa_{\mathrm{GNDwall}}(\mathrm{r}_1)\tau_{\mathrm{wall}}(\mathrm{r} - \mathrm{r}_1)\mathrm{d}\mathrm{r}_1, \tag{8}$$

where Ω represents the volume of the coarse-graining element.

In the proposed convolution formulation, the term $\kappa_{\mathrm{GNDwall}}(\mathrm{r}_1)$ represents the density of GND walls at position r_1, while $\tau_{\mathrm{wall}}(\mathrm{r} - \mathrm{r}_1)$ denotes the stress field at the position r induced by a single GND wall at position r_1. The product of $\kappa_{\mathrm{GNDwall}}(\mathrm{r}_1)$ and $\mathrm{d}r_1$ corresponds to the total number of GND walls within a small distance segment $\mathrm{d}r_1$. By integrating the product over the entire element domain Ω, the convolution yields the effective stress at position r induced by the heterogeneous distribution of GND walls within the coarse-graining volume. To fully determine the nearfield correction stress field, the functional forms of $\kappa_{\mathrm{GNDwall}}(\mathrm{r})$ and $\tau_{\mathrm{wall}}(\mathrm{r})$ need to be specified.

In this study, we adopt the formulation $\tau_{\mathrm{wall}}(\mathrm{r} - \mathrm{r}_1)$ for the stress field induced by a single GND wall at position r_1 based on Hirth and Lothe (1982). The stress caused by a GND wall can be derived from the superposition of individual edge dislocations within the wall. To address the divergence behavior near the core region of the GND wall, we employ

the integration form proposed by Roy et al. (2008). The explicit form of $\tau_{\text{wall}}(\mathrm{r}-\mathrm{r}_1)$ is given by:

$$\tau_{\text{wall}}(\mathrm{r}-\mathrm{r}_1)=\frac{\mu\,|b|}{2\pi(1-\nu)}\frac{\mathrm{L}(\mathrm{r}-\mathrm{r}_1)}{\mathrm{L}^2+(\mathrm{r}-\mathrm{r}_1)^2}. \tag{9}$$

It is important to remark that the direct resolution of $\kappa_{\text{GNDwall}}(\mathrm{r})$ through experimental or theoretical methods is currently not feasible. Thus, we assume that it can be expressed as the product of the total number of dislocation walls, denoted as $\mathrm{N_x}$, and the probability density function, denoted as $d(\mathrm{r})$. This assumption allows us to control the overall quantity of GNDs within the coarse-graining by adjusting $\mathrm{N_x}$, while $d(\mathrm{r})$ governs the shape of the inhomogeneous distribution. Assuming the coarse-graining has the same length along both the x and y directions, $\mathrm{N_x}$ is therefore assumed to be the same as $\mathrm{N_y}$. The factors influencing the probability density function $d(\mathrm{r})$ are assumed to include the position within a coarse-graining r, the element size ℓ, the gradient of dislocation density crossing the element $\nabla\rho$, which accounts for the influence of adjacent coarse-graining elements, and the microstructure within the coarse-graining volume, including ρ_{SSD}, ρ_{GND}, and ρ_{tot}. Notably, when considering the gradient of dislocation density $\nabla\rho$, it is crucial to consider the gradient of GND rather than SSD density. This finding is supported by Fig. 3, where it is evident that the impact of dislocation dipoles is limited to a short range, resulting in a negligible influence from the SSDs present in adjacent elements on the heterogeneity distribution within the targeted element. Hence, we consider only the influence of $\nabla\rho_{\text{GND}}$, and the formulation of $\kappa_{\text{GNDwall}}(\mathrm{r})$ can be represented as:

$$\kappa_{\text{GNDwall}}(\mathrm{r})|_{\mathrm{r}\in\Omega}=\mathrm{N_x}\cdot d(\mathrm{r},\ell,\nabla\rho_{\text{GND}},\rho_{\text{SSD}},\rho_{\text{GND}},\rho_{\text{tot}}), \tag{10}$$

where r resides within the range of the coarse-graining volume Ω. Regarding the determination of the probability density function $d(\mathrm{r},\ell,\nabla\rho_{\text{GND}},\rho_{\text{SSD}},\rho_{\text{GND}},\rho_{\text{tot}})$, we employ a statistical analysis of a large dataset generated from extensive DDD simulations within Section 4.

4. Statistical Analysis of the Distribution Function for Heterogeneity

Based on the results in Section 3, within this section, a statistical approach is employed to obtain the distribution function $d(\mathrm{r},\ell,\nabla\rho_{\text{GND}},\rho_{\text{SSD}},\rho_{\text{GND}},\rho_{\text{tot}})$ of Eq. (10) for the GND walls withing coarse-graining. Generating a dataset of GND wall distribution under various combinations of state variables by the DDD simulation, we utilize a neural network to conduct sensitivity tests confirming the impact of each state variable on heterogeneity formations. Finally, the formulation of the probability density function is derived in a way appropriate for incorporation into the nearfield correction stress formulation.

4.1. Statistical Dataset Generation

In order to generate the dataset required for deriving the probability density function within Eq. (10), we conduct a series of benchmarked DDD simulations. Each simulation follows the setup outlined in Section 2. Through the manipulation of the number of positive and negative dislocations within the three elements, along with adjusting the sizes of these elements, we systematically explore the heterogeneous distribution of GND walls under various combinations of associated state variables. These adjusted variables, which correspond to the variables of continuum theories, include the element size ℓ representing the numerical length scale that measures the level of discretization for coarse-graining. Additionally, we consider the state variables being representative of microstructures, such as $\nabla\rho_{\text{GND}}$, ρ_{SSD}, ρ_{GND}, and ρ_{tot}.

As discussed in Section 3.2, τ^{ξ}_{nfc} considers the internal stress of the heterogeneity within the coarse-graining, thus, the interaction across slip systems should play a minor role on influencing the heterogeneity features within the coarse-graining. The effects induced by the interaction between different slip systems might have a significant influence on the local stress field but a detailed incorporation based on discrete considerations go beyond the scope of this paper and is supposed to be further considered by the yield stress term in Eq. (7). Moreover, there are often single slip systems more active in forming pileups in the region close to grain boundaries or precipitates. Therefore, the single-slip DDD simulation can serve as a meaningful tool for deriving the distribution function for the GND walls within the coarse-graining volumes. Insights into single-slip processes can therefore lead to a fundamental understanding that is also helpful for a better evaluation of interaction in complex three-dimensional configurations.

Within this study, we aim at the derivation of the correction stress for the microstructure heterogeneity in the transition regime from discrete to continuum simulations. To construct a representative dataset for statistical derivation,

Table 1
The summary of simulated length scale for discrete dislocation dynamic.

reference	initial dislocation density(μm^{-2})	system size(μm)
Zbib et al. (1998)	21	3
Arsenlis et al. (2007)	1.8	15
Motz et al. (2009); Weygand et al. (2008)	20	$0.5 \sim 1$
Zhou et al. (2010)	$2 \sim 25$	$0.5 \sim 1$
Hussein et al. (2015)	$0.5 \sim 10$	10
Sills et al. (2018)	0.7	15
Zhang et al. (2021)	100	0.6

we investigate the range of system sizes and dislocation densities that are commonly employed in DDD simulations summarized in Table 1. The range of dislocation densities for our dataset encompasses an expansion from $10^1 \mu m^{-2}$ to $10^2 \mu m^{-2}$, starting from a commonly observed initial dislocation density in the referenced DDD simulations and extending two orders higher to cover up the dislocation density of a deformed material. This range of dislocation density is also consistent with experimental observations (e.g., Jiang et al. (2013)). The system sizes from $10\mu m$ to $100\mu m$ are commonly explored not only in discrete simulations but also in continuum-scale simulations (e.g., Fleck et al. (1994); Chong et al. (2001); Tagarielli and Fleck (2011); Wulfinghoff et al. (2013); Bardella and Panteghini (2015); Guo et al. (2017)). Therefore, we select reasonable discretization levels ensuring the coarse-graining size, ℓ, one to two orders smaller than the overall system size. Regarding the range of $\nabla\rho_{\mathrm{GND}}$, it is automatically determined once the dislocation density and element size are fixed.

To sum up the ranges of each variable, we assume six levels for the values of ρ_{SSD} and ρ_{GND} within the range $\{10, 20, 40, 60, 80, 100\}\mu m^{-2}$, five levels for $\nabla\rho_{\mathrm{GND}} \in \{20, 40, 60, 80, 100\}\mu m^{-3}$, and three levels for $\ell \in \{0.5, 1, 1.5\}\mu m$. As a result, for each element size, we conduct DDD simulations, generating a total of 180 combinations of state variables. For each combination of state variables, a minimum of 20 DDD simulations were conducted to estimate the probability of GND wall formation at each position within the coarse-graining volume. All simulations were controlled to maintain consistent state variables, while the initial seeding varied following a random distribution. This yields a DDD dataset comprising a total of 10859 simulations.

The simulated results obtained from each combination of state variables undergo a post-processing procedure. To illustrate the post-processing procedure of the DDD simulation data, as an example, we examine the 20 resulting targeted elements, which have the same dislocation quantity and element size as the setup shown in Fig. 1. The post-processing procedure comprises two main steps: SSD filtering and GND wall identification, as depicted in Fig. 5(a) and (b).

In the SSD filtering step, the goal is to enhance the identification of GND walls by excluding SSD. To achieve this, a criterion based on the angle between pairs of dislocations with different signs is employed. Specifically, if the angle between two dislocations falls within the range of -45 degrees to 45 degrees (depicted as the gray triangle regions in Fig. 5 (a)), they are identified as part of a dipole structure and are excluded. After applying the SSD filtering, the post-processing procedure for GND wall identification is presented in Fig. 5 (b). This procedure involves calculating the probability of GND wall formation at different positions within the coarse-graining volume. To achieve this, the coarse-graining volume is divided into multiple bins along the r-direction (see Fig. 5 (b)). The number of excess edge dislocations within each bin is quantified. A GND wall structure is considered to form if the count of excess dislocations surpasses a threshold value. In this study, we assume the threshold value is equivalent to Ny, based on the assumed configuration of coarse-graining for continuous theories as depicted in Fig. 4. The bin size, ℓ_{bin}, is equal to the length of the attraction zone near a edge dislocation wall, as derived by Li (1960):

$$\ell_{\mathrm{bin}} = \frac{\mathrm{L}}{\pi} \ln\left(\pi\sqrt{\mathrm{n}}\right), \tag{11}$$

where n represents the number of edge dislocations within the finite wall, which is equivalent to $\mathrm{N_y}$. The choice of ℓ_{bin} as the value of the attraction zone adjacent to a GND wall is due to the fact that dislocations within this region are attracted to the GND wall rather than being repelled. Therefore, positive dislocations within this attraction zone are considered as part of the GND wall. The position of each bin is defined as the distance from the right end of the coarse-graining volume to the center of the bin, as illustrated in Fig. 5(b). The right end of the coarse-graining volume

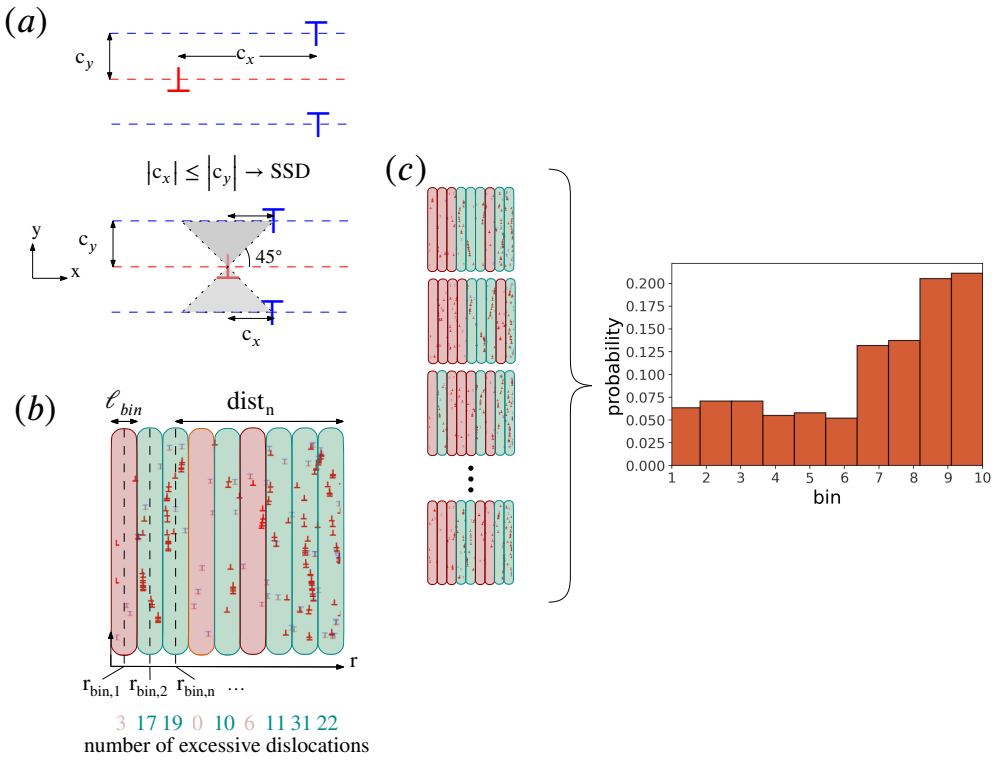

Figure 5: Schematic visualization of the post-processing steps and GND wall probability derivation. (a) SSD Filtering: This step excludes SSDs to enhance the identification of GND walls. Dislocations with different signs that form an angle between -45 degrees and 45 degrees are considered dipole structures and are disregarded in the analysis. (b) GND Wall Identification: After the SSD filtering, the remaining excess dislocations are analyzed within bins of length ℓ_{bin}. Bins with an excess dislocation number surpassing N_y are identified as regions where GND walls exist and are shown in green. Bins with a lower count indicate the absence of GND walls and are shown in red. (c) GND Wall Probability: The results from each 20 DDD simulations with the same parameter configuration are combined to derive the probability of encountering a GND wall within each coarse-graining volume. This is accomplished by calculating the frequency of GND wall occurrence across all simulations.

corresponds to the side adjacent to a higher GND density element. The position of the center of bin n is defined by $r_{\text{bin,n}}$, the distance of bin n to the right end of the coarse-graining volume is denoted as $dist_n = \ell - r_{\text{bin,n}}$.

After the identification of GND walls within each coarse-graining volume through the post-processing steps, we proceed to calculate the probability of finding a GND wall at each bin, as depicted in Fig. 5(c). By following the aforementioned procedure, we generate a dataset that contains the probability of finding a GND wall as the dependent variable. The independent variables in this dataset include the state variables, namely $\nabla\rho_{\text{GND}}$, ρ_{SSD}, ρ_{GND}, ρ_{tot}, and $dist$.

4.2. Neural Network Analysis for Identifying Independent Variables

Following the methodology outlined in Section 4.1, we generate a dataset that spans the transition from discrete to continuous theory. However, the exact formulation of the function d still remains unknown. To examine the impact of each independent variable on the probability, we employ neural network analysis as a sensitivity test to identify the influence of independent variables.

The network architecture employed in training the dense neural network models is shown in Fig. 6. We use Keras (Chollet et al. (2015) to construct and train our model. The architecture consists of three densely connected layers. The initial layer comprises 64 units and uses the rectified linear activation function (ReLU) to introduce non-linearity. Following standard practice, batch normalization is applied after each hidden layer to enhance training stability. The subsequent hidden layer has 32 units also activated by ReLU keeping the possibility of non-linearity. The final layer, consisting of a single unit, employs the sigmoid activation function to generate a probability-like output. The model is

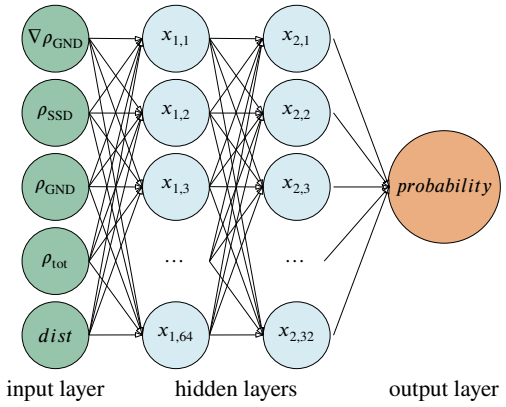

Figure 6: Neural network model trained for identifying the independent variables having the highest impact comprises five inputs, two hidden layers of 64 and 32 neurons respectively, and an output layer with one output.

optimized using the Adam optimizer, and its performance is assessed using the mean squared error loss function. The performance of the models is then assessed using two approaches: ground truth validation and regression distribution analysis. By alternating different combinations of variables in the input layer, the impact of independent variables can be analyzed based on the quality of the trained neural network model.

In the ground truth validation, the R^2 (coefficient of determination) is calculated to measure the error between the predicted probabilities and the actual observed values from the DDD simulations. In this study, the R^2 is calculated by

$$R^2 = 1 - \frac{\sum(p_{obs} - p_{pred})^2}{\sum(p_{obs} - \bar{p}_{obs})^2}, \tag{12}$$

where p_{obs} represents the observed values of the dependent variable, p_{pred} represents the predicted values of the dependent variable, and $\bar{p}_{obs}$ represents the mean of the observed values. Additionally, the root mean squared error (RMSE) serves as a complementary metric to further assess the accuracy and precision of the prediction models. The RMSE is calculated by

$$RMSE = \sqrt{\frac{1}{n}\sum_{i=1}^{n}(p_{obs} - p_{pred})^2} \tag{13}$$

where p_{obs} represents the observed values of the dependent variable, p_{pred} denotes the predicted values of the dependent variable, and n is the number of data points.

The performance of the neural network model, which was trained using all five independent parameters in the input layer (as depicted in Fig. 6), is shown in Fig. 7. Fig. 7 (a) illustrates the ground truth validation results, where the R^2 value is 0.6760, indicating a moderate level of correlation between the predicted values and the actual ground truth values. The RMSE has a value of 0.0271. Fig. 7 (b) showcases the distribution of residual errors, which are centered slightly smaller than zero. These results suggest that the neural network model, trained using all five independent variables together, achieves an approximate average error of 2.7% in determining the probability of predicting the formation of a GND wall. The residual errors are randomly distributed around the true values but slightly smaller than zero, indicating that the model tends to slightly underestimate the predictions.

To categorize the independent variables based on their length scales, $\nabla\rho_{GND}$ has the largest length scale, as it involves the influence across the elements. On the other hand, $dist$ has the smallest length scale, capturing spatial discretization within the coarse-graining. In terms of the dislocation densities, ρ_{SSD}, ρ_{GND}, and ρ_{tot} exhibit similar length scales. In order to investigate the influence of different dislocation densities, specifically $\rho_{SSD}, \rho_{GND}, \rho_{tot}$, we conduct an analysis focusing on neural network models that utilize only three independent parameters. We kept the two independent variables $\nabla\rho_{GND}$ and $dist$ fixed in the input layer, and varied the included dislocation densities to assess their impact on predicting the probability of GND wall formation. The ground truth validation results are

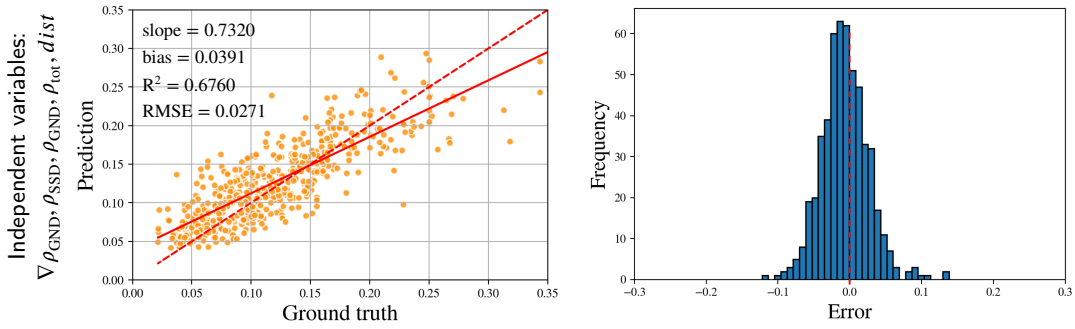

Figure 7: The figure demonstrates the performance of the neural network model trained by all five independent variables. (a) presents the results of the ground truth validation. The red dashed lines represent the ideal prediction along a 45-degree line. (b) illustrates the distribution of residuals

shown in Fig. 8a to Fig. 8e. From Fig. 8a, the model trained with ρ_{SSD} achieves an R^2 value of 0.6747, indicating that approximately 67.47 % of the variance in the dependent variable can be explained by this model. The RMSE value of 0.0336 suggests that the average error in the predicted probabilities is 3.36 %. The ground truth validation results shown in Fig. 8a shows the model trained with ρ_{SSD} has nearly equal performance as the model trained with all five independent parameters based on the quantity of R^2 and RMSE, and has noticeably better performance than the models trained with ρ_{GND} or ρ_{tot}, which both show low R^2 values of $\approx$ 0.3. The regression distribution analysis visualizes the error distributions of the trained models and is shown in Fig. 8b to Fig. 8f. In the case of the model trained with ρ_{SSD}, the error distribution follows a normal distribution with a spread of approximately 0.1 centering at zero. On the other hand, the models trained with ρ_{GND} and ρ_{tot} exhibit a rightward tail in their error distributions. This means that the models trained with ρ_{GND} or ρ_{tot} consistently predict lower probabilities compared to the actual probabilities and therefore both have systematic underpredictions.

As part of the investigation, we have carefully explored various model architectures to understand whether different neural network architecture influences the sensitivity patterns observed. Upon analyzing the results, we observed that while there were some minor variations in sensitivity, the overarching trends and relationships between input variables and predictions remained consistently aligned. Therefore, we choose the model which shows the best performance for the analysis.

Summarizing, the models trained with only three independent variables, namely $\nabla\rho_{GND}$, ρ_{SSD}, and $dist$, demonstrate comparable prediction performance to the model trained with all five variables. This indicates that these three variables are nearly sufficient to predict the probability of the GND wall formation within a coarse-graining. The potential influence of other state variables, other than the five selected variables, on the prediction of probability is beyond the scope of this study.

4.3. Formulation of the Probability Density Function

As an initial guess, the formulation of the probability density function $d(\mathrm{r})$ is motivated by the classical back stress formulation in the context of work-conjugated gradient plasticity theory (e.g., Aifantis (1984); Gurtin (2002)). Building upon these theoretical foundations, we postulate that the distribution function $d(\mathrm{r})$ is proportional to the gradient of the GND density $\nabla\rho_{GND}$ and the square of the material length scale l^2, so it holds

$$d \propto l^2 \nabla \rho_{GND}. \tag{14}$$

Although the relationship between microstructure and the material length scale within work-conjugated gradient plasticity theory remains uncertain as discussed within Section 1, we adopt the finding by Berdichevsky (2006) that the material length scale should be approximated by a kind of dislocation density maintaining the consistency of units.Therefore, we can express Eq. (14) as:

$$d \propto \frac{\nabla \rho_{GND}}{\rho}, \tag{15}$$

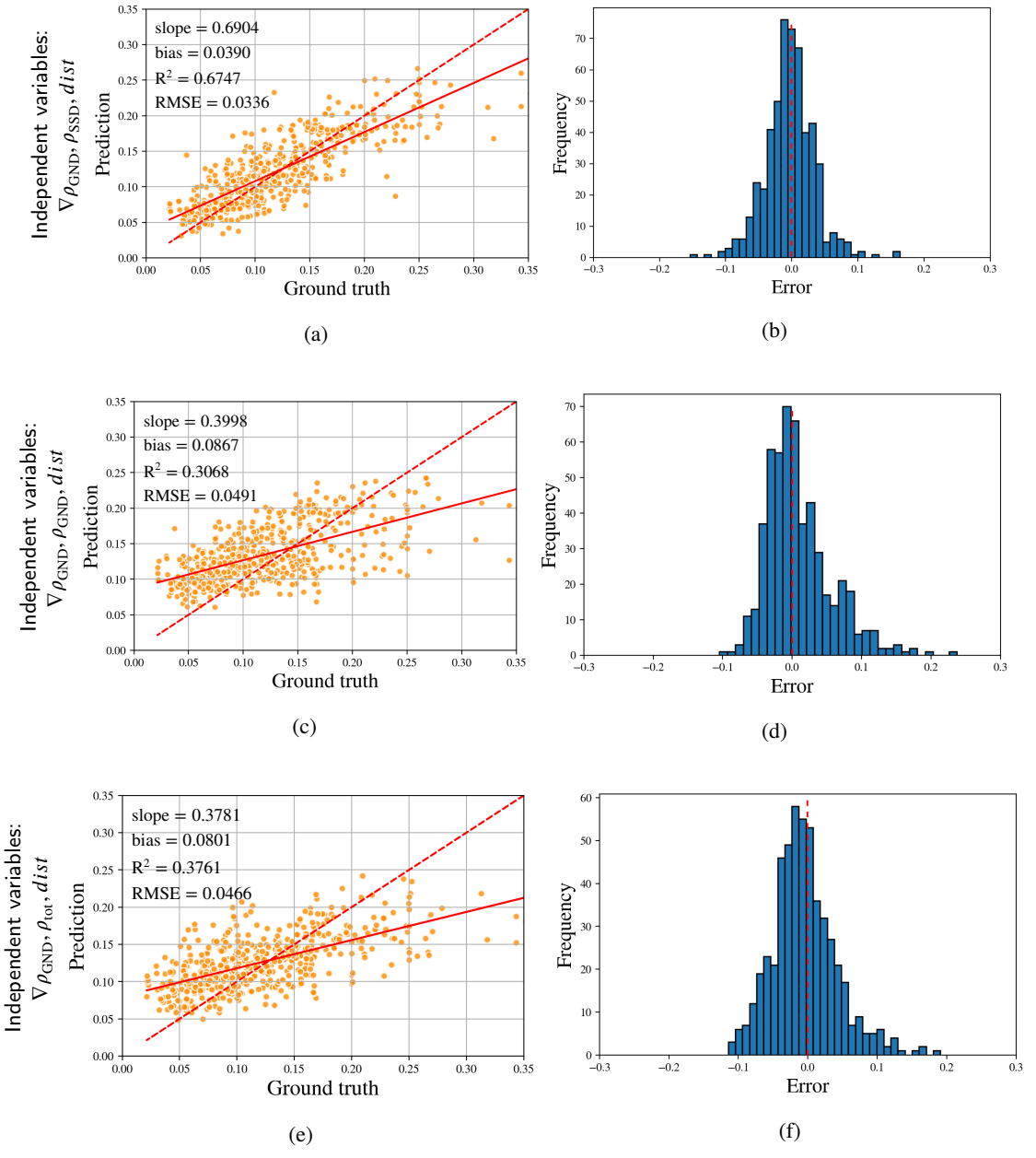

Figure 8: Performance evaluation of neural network models trained using different combinations of independent parameters. The adopted independent variables are as listed. (a) and (b) were trained with the ρ_{SSD} as the independent parameter, models (c) and (d) utilized the ρ_{GND}, and models (e) and (f) employed the ρ_{tot}. Ground truth validation results are shown in (a), (c), and (e), in which the red dashed lines represent the perfect prediction of a 45-degree line, and the red solid line indicates the fitted curve between the predicted values and the ground truth. Regression error distribution analysis is depicted in (b), (d), and (f).

where ρ represents the dislocation density, which can be any type, including ρ_{SSD}, ρ_{GND}, or ρ_{tot}. The performance evaluation of the neural network models, as presented in Section 4.2, lead to the conclusion that the inclusion of ρ_{SSD} in the formulation is deemed more suitable. By observing the results shown in Fig. 5, it is evident that the likelihood of encountering a GND wall tends to be higher along the direction of the gradient of GND density. Therefore, we propose that the probability of GND wall formation is inversely proportional to the parameter $dist$. Therefore, Eq. (15) can be

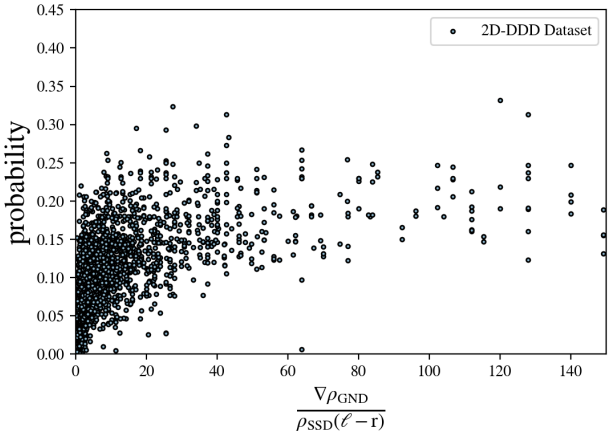

Figure 9: The scatter plot between the probability and $\frac{\nabla\rho_{GND}}{\rho_{SSD}(\ell-r)}$.

written as

$$d \propto \frac{\nabla\rho_{GND}}{\rho_{SSD} \cdot dist} = \frac{\nabla\rho_{GND}}{\rho_{SSD}(\ell - r)}. \tag{16}$$

The linear relationship between probability and $\frac{\nabla\rho_{GND}}{\rho_{SSD}(\ell-r)}$ is plotted in Fig. 9, it is observed that there is a logarithmic dependency between the probability and the parameter $\frac{\nabla\rho_{GND}}{\rho_{SSD}(\ell-r)}$. Therefore, we propose the function d to be:

$$d = C \ln\left(1 + \frac{\nabla\rho_{GND}}{\rho_{SSD}(\ell - r)}\right), \tag{17}$$

where C is a constant that can be determined through linear regression fitting. We additionally shift the value of $\frac{\nabla\rho_{GND}}{\rho_{SSD}(\ell-r)}$ by 1 to avoid negative values induced by the logarithmic dependency. The result of a processed curve fitting of the dataset is shown in Fig. 10. Herein, the dataset generated by DDD simulations is represented as points in Fig. 10a, and the fitted result is indicated by the red line, with a value of C determined as 0.0588. The R^2 value, is 0.5177, and the RMSE, is 4 %. The regression error betweeen the data points and the red curve in Fig. 10a is depicted in Fig. 10b, and the histogram is shown in Fig. 10c. The regression histogram exhibits a normal distribution centered around zero, indicating a reasonable fit of the proposed function. The error distribution follows a normal distribution with a spread of approximately 0.1, which is similar to the best model we trained within neural network analysis. From the value of RMSE and the normally distributed regressions, we can conclude that the prediction quality of the function d proposed in Eq. (17) is comparable to that of the best neural network model trained. The scatterness induced by the error between the predicted value and the dataset can be attributed to the nature of random initial seeding of the DDD simulations as well as the potential influence of other factors that are not considered within this study.

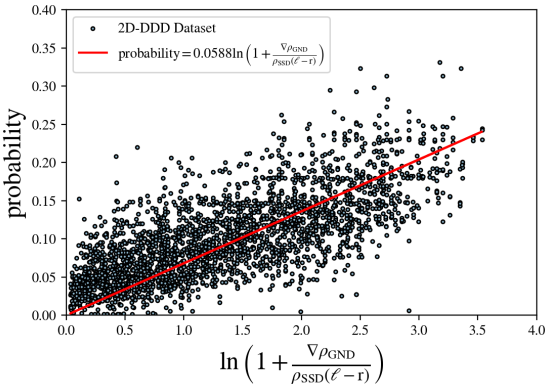

(a)

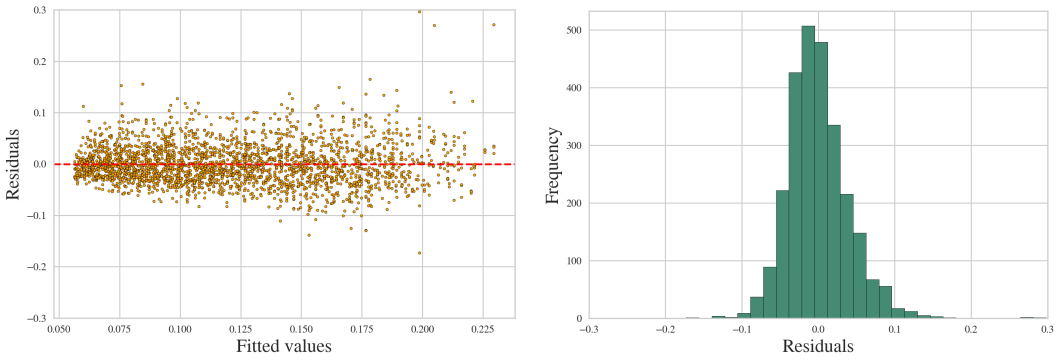

(b) (c)

Figure 10: Linear fitting results of Eq. (17), including (a) scatter plot with all DDD data, the red line indicating the best fit, (b) regression error distribution plot, and (c) histogram of the regression error.

5. Internal Stress in the Discrete-to-Continuum Transition Regime

In this section, we first demonstrate the effect of different dislocation densities on the distribution of the GND walls to elaborate their impact on the distribution of heterogeneity. Moreover, we derive the nearfield correction stress $\tau^{\xi}_{\mathrm{nfc}}$ based on the presumed formulation within Section 3, and incorporated the probability density function derived within Section 4.

5.1. Influence of Dislocation Densities on the Heterogeneity

Based on the findings in Section 4.2, the importance of the dislocation density ρ_{SSD} in predicting probabilities of the existence of a GND wall has been identified. In order to further validate the finding, this section focuses on investigating the results of microstructure heterogeneity obtained from the DDD dataset. The aim is to demonstrate how the distribution of microstructure heterogeneity within a coarse-graining volume is influenced by the three types of dislocation densities: ρ_{SSD}, ρ_{GND}, and ρ_{tot}.

From the DDD dataset generated in Section 4.1, as a case study, we examine the configurations with ℓ equals to $1\mu m$ and $\nabla\rho_{\mathrm{GND}}$ equals to $60\mu m^{-3}$. The total dislocation density ρ_{tot} varies from $80\mu m^{-2}$ to $160\mu m^{-2}$. We analyze two cases to explore the impact of different dislocation densities: (1) Controlling the value of ρ_{SSD} as a constant and varying the value of ρ_{GND}. (2) Controlling the value of ρ_{GND} as a constant and varying the value of ρ_{SSD} . The results are shown in Fig. 11, see the upper row in Fig. 11 for case (1) and lower row in Fig. 11 for case (2).

For a further comparison, the heterogeneous microstructure and stress field within the coarse-graining volumes for cases (2) are shown in Fig. 12. Examples for high and low values of ρ_{SSD}, corresponding to one of the leftmost and rightmost cases from the lower row of Fig. 11 are depicted. The relaxed heterogeneous microstructures for high and

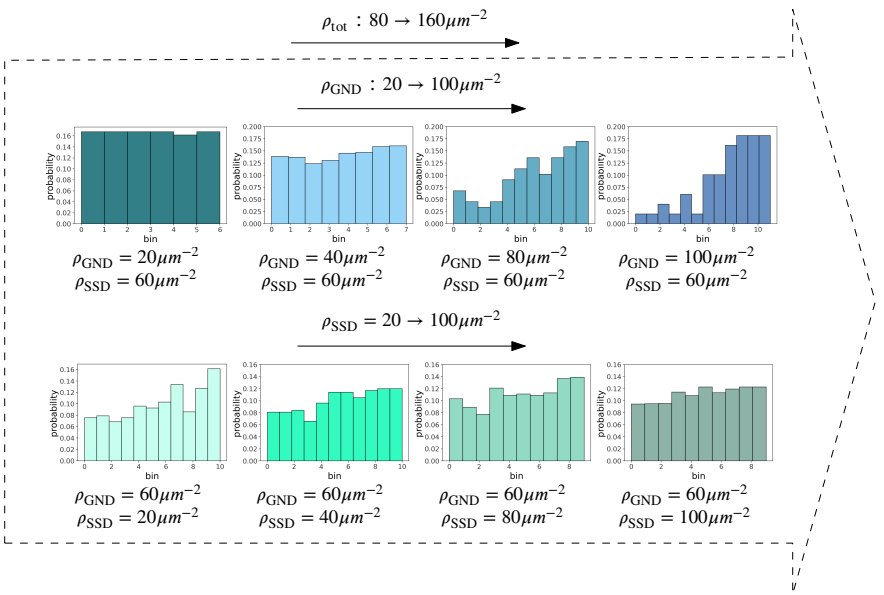

Figure 11: The impact of different ρ_{GND}/ρ_{SSD} relations on the probability of GND wall formation for a variation of ρ_{tot} from $80\mu m^{-2}$ to $160\mu m^{-2}$ on the heterogeneity within a coarse-graining volume for an element size of 1 μm. The upper row keeps a constant ρ_{SSD}; the lower row keeps a constant ρ_{GND}.

low amounts of SSDs can be observed in Fig. 12a and Fig. 12b respectively. The corresponding internal stress field is given in Fig. 12c and Fig. 12d.

5.2. The Nearfield Correction Stress

Combining the presumed formulation of the nearfield correction stress discussed within Section 3 and the data-based derivation for the probability distribution of the heterogeneity within Section 4, we insert Eq. (17) into Eq. (10), then, together with Eq. (9) into Eq. (8). The nearfield correction stress can thus be written as,

$$\tau^{\xi}_{nfc} = \int_{\Omega} \overbrace{\ell\sqrt{\rho_{GND}}\cdot 0.0588\ln(1+\mathcal{X})}^{\text{GND wall density function, } \kappa_{GNDwall}(r_1)(\text{see } Eq.\ (10))} \underbrace{\frac{\mu\,|b|}{2\pi(1-\nu)}\frac{L(r-r_1)}{L^2+(r-r_1)^2}}_{\text{stress field created by a GND wall, } \tau_{wall}(r-r_1)(\text{see } Eq.\ (9))} dr_1, \tag{18}$$

where

$$\mathcal{X} = \frac{\nabla\rho_{GND}}{\rho_{SSD}(\ell - r)}. \tag{19}$$

However, it becomes obvious that the formulation is not integrable in its current form. To address this issue, we introduce two expansion methods: the Maclaurin series expansion for cases where $\mathcal{X}$ is less than 1, and the Puiseux series expansion for cases where $\mathcal{X}$ is larger than 1.

When $\mathcal{X} < 1$, we can approximate the probability density function of the GND wall density using the Maclaurin series. Denoting $d_{Maclaurin}(r)$, it can be expressed as:

$$d_{Maclaurin}(r) \approx 0.0588\left(\mathcal{X} - \frac{\mathcal{X}^2}{2} + \frac{\mathcal{X}^3}{3} - \cdots\right). \tag{20}$$

Considering only the first-order term, the truncation error $\mathcal{E}_{Maclaurin}$ is given by:

$$\mathcal{E}_{Maclaurin} = \frac{1}{2}\left(\frac{\nabla\rho_{GND}}{\rho_{SSD}(\ell - r)}\right)^2 = \frac{1}{2}\mathcal{X}^2. \tag{21}$$

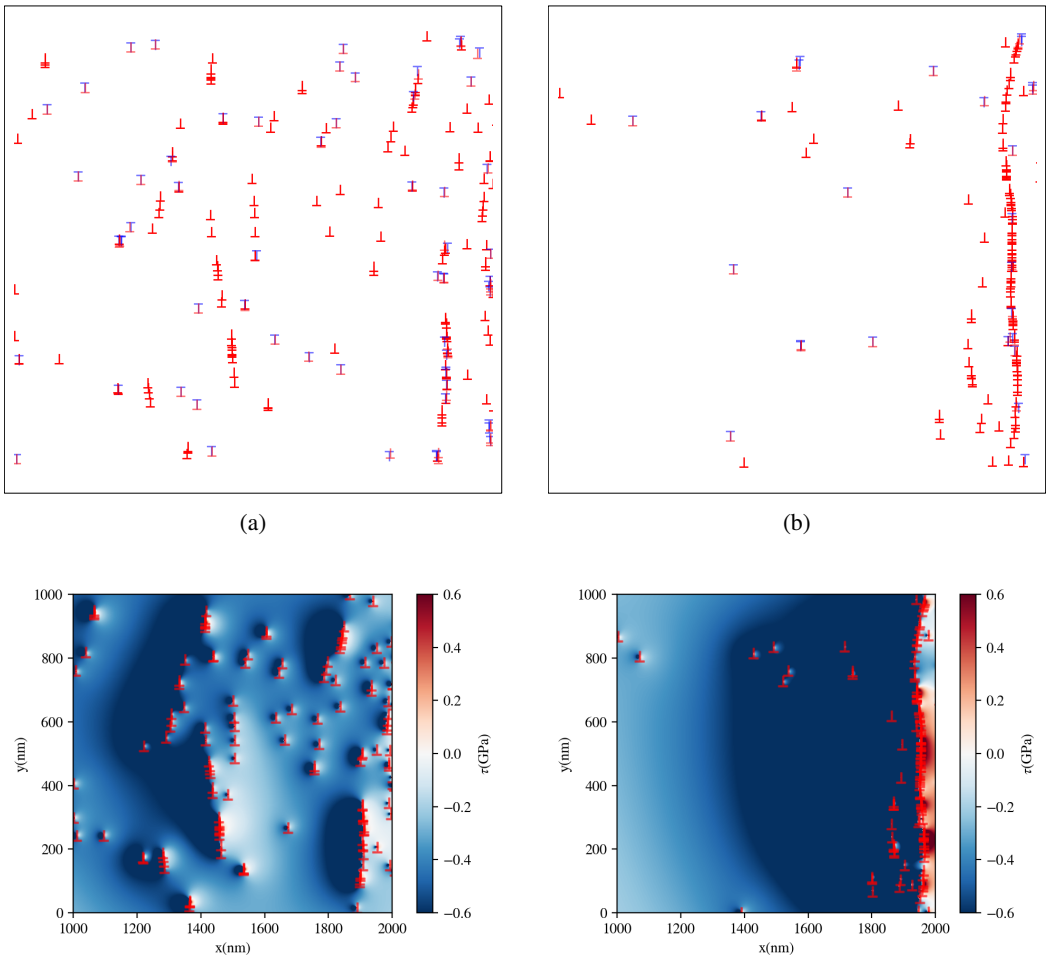

Figure 12: The comparison between the cases of high and low ρ_{SSD} values: (a) represents the resulting heterogeneity within Element 2 when ρ_{SSD} is set to $100\mu m^{-2}$. (b) represents the resulting heterogeneity within Element 2 when ρ_{SSD} is set to $20\mu m^{-2}$. (c) represents the resulting stress field induced by (a). (d) represents the resulting stress field induced by (b).

This approximation allows us to compute the GND wall density function as the value of $\mathcal{X}$ is small, with the truncation error proportional to $\mathcal{X}^2$. Therefore, the expression for τ^{ξ}_{nfc} of Eq. (8) in the case of $\mathcal{X} < 1$ can be given by:

$$\tau^{\xi}_{nfc,\mathcal{X}<1} = \frac{\mu\,|b|}{2\pi(1-\nu)} \int_{\Omega} \ell \sqrt{\rho_{GND}} \cdot 0.0588 \left(\frac{\nabla\rho_{GND}}{\rho_{SSD}}\right) \left(\frac{1}{(\ell - r_1)}\right) \frac{L(r-r_1)}{L^2 + (r-r_1)^2} dr_1. \tag{22}$$

To separate the parts independent of the integration variable r_1, we have:

$$\tau^{\xi}_{b,\mathcal{X}<1} = \frac{\mu\,|b|}{2\pi(1-\nu)} \ell \sqrt{\rho_{GND}} \cdot 0.0588 \left(\frac{\nabla\rho_{GND}}{\rho_{SSD}}\right) \int_{\Omega} \frac{L(r-r_1)}{(\ell - r_1)[L^2 + (r-r_1)^2]} dr_1. \tag{23}$$

Finally, by integrating the formulation within the range of a coarse-graining volume, i.e., $r_1 \in (0, \ell)$, the expression becomes:

$$\tau^{\xi}_{b,\mathcal{X}<1} = \frac{\mu\,|b|}{2\pi(1-\nu)} \cdot 0.0588 \ell \sqrt{\rho_{GND}} \left(\frac{\nabla\rho_{GND}}{\rho_{SSD}}\right) \arctan\left(\frac{\ell}{L}\right) \tag{24}$$

$$= \frac{\mu\,|b|}{2\pi(1-\nu)} D' \left(\frac{\nabla\rho_{GND}}{\rho_{SSD}}\right), \tag{25}$$

where D' is an associated material parameter that depends on both ℓ and ρ_{GND}:

$$D' = 0.0588\ell\sqrt{\rho_{\mathrm{GND}}}\arctan\left(\ell\sqrt{\rho_{\mathrm{GND}}}\right). \tag{26}$$

It should be noted that the formulation of the back stress term, derived from applying the Maclaurin series, has a linear dependency on $\frac{\nabla\rho_{\mathrm{GND}}}{\rho_{\mathrm{SSD}}}$ similar to the classical back stress terms within continuous crystal plasticity. This characteristic has been discussed in previous studies by Aifantis (1984); Gurtin (2002).

For the case $\mathcal{X} \geq 1$, a Puiseux series expansion can be employed when $\mathcal{X}$ exceeds 1. The expansion of the GND wall density function, denoted as $d_{\mathrm{Puiseux}}(\mathrm{r})$, is written then by:

$$d_{\mathrm{Puiseux}}(\mathrm{r}) \approx 0.0588\left(\ln\mathcal{X} + \frac{1}{\mathcal{X}} - \frac{1}{2\mathcal{X}^2} + \frac{1}{3\mathcal{X}^3} - \cdots\right). \tag{27}$$

When truncating the expansion at the first order, the truncation error $\mathcal{E}_{\mathrm{Puiseux}}$ for the Puiseux series expansion is given by:

$$\mathcal{E}_{\mathrm{Puiseux}} = \frac{1}{\mathcal{X}} = \frac{\rho_{\mathrm{SSD}}(\ell - \mathrm{r})}{\nabla\rho_{\mathrm{GND}}}. \tag{28}$$

Thus, for $\mathcal{X} \geq 1$, the expression for $\tau^{\xi}_{\mathrm{nfc}}$ becomes:

$$\tau^{\xi}_{\mathrm{nfc},\mathcal{X}\geq 1} = \frac{\mu\,|b|}{2\pi(1-\nu)}\int_{\Omega}\ell\sqrt{\rho_{\mathrm{GND}}}\cdot 0.0588\ln\left(\frac{\nabla\rho_{\mathrm{GND}}}{\rho_{\mathrm{SSD}}(\ell-\mathrm{r}_1)}\right)\frac{\mathrm{L}(\mathrm{r}-\mathrm{r}_1)}{\mathrm{L}^2+(\mathrm{r}-\mathrm{r}_1)^2}\mathrm{d}\mathrm{r}_1 \tag{29}$$

$$= \frac{\mu\,|b|}{2\pi(1-\nu)}\ell\sqrt{\rho_{\mathrm{GND}}}0.0588\left[\int_{\Omega}\ln\left(\frac{\nabla\rho_{\mathrm{GND}}}{\rho_{\mathrm{SSD}}}\right)\frac{\mathrm{L}(\mathrm{r}-\mathrm{r}_1)}{\mathrm{L}^2+(\mathrm{r}-\mathrm{r}_1)^2}\mathrm{d}\mathrm{r}_1 - \int_{\Omega}\ln\left(\frac{1}{(\ell-\mathrm{r}_1)}\right)\frac{\mathrm{L}(\mathrm{r}-\mathrm{r}_1)}{\mathrm{L}^2+(\mathrm{r}-\mathrm{r}_1)^2}\mathrm{d}\mathrm{r}_1\right] \tag{30}$$

$$= \frac{\mu\,|b|}{2\pi(1-\nu)}\ell\sqrt{\rho_{\mathrm{GND}}}0.0588\left[\ln\left(\frac{\nabla\rho_{\mathrm{GND}}}{\rho_{\mathrm{SSD}}}\right)\int_{\Omega}\frac{\mathrm{L}(\mathrm{r}-\mathrm{r}_1)}{\mathrm{L}^2+(\mathrm{r}-\mathrm{r}_1)^2}\mathrm{d}\mathrm{r}_1 - \int_{\Omega}\ln\left(\frac{1}{(\ell-\mathrm{r}_1)}\right)\frac{\mathrm{L}(\mathrm{r}-\mathrm{r}_1)}{\mathrm{L}^2+(\mathrm{r}-\mathrm{r}_1)^2}\mathrm{d}\mathrm{r}_1\right] \tag{31}$$

$$= \frac{\mu\,|b|}{2\pi(1-\nu)}\ell\sqrt{\rho_{\mathrm{GND}}}0.0588\left[\ln\left(\frac{\nabla\rho_{\mathrm{GND}}}{\rho_{\mathrm{SSD}}}\right)\frac{\mathrm{L}}{2}\ln\left(\frac{\mathrm{L}^2+\ell^2}{\mathrm{L}^2}\right) - \mathrm{L}\left[\frac{\ln(\ell)\ln\left(\frac{\mathrm{L}^2+\ell^2}{\mathrm{L}^2}\right)}{2} + \frac{\mathrm{Li}_2\left(-\frac{\ell^2}{\mathrm{L}^2}\right)}{4}\right]\right] \tag{32}$$

$$= \frac{\mu\,|b|}{2\pi(1-\nu)}\ell\sqrt{\rho_{\mathrm{GND}}}0.0588\left[\frac{\mathrm{L}}{2}\ln\left(\frac{\nabla\rho_{\mathrm{GND}}}{\rho_{\mathrm{SSD}}}\right)\ln\left(\frac{\mathrm{L}^2+\ell^2}{\mathrm{L}^2}\right) - \frac{\mathrm{L}}{2}\left[\ln(\ell)\ln\left(\frac{\mathrm{L}^2+\ell^2}{\mathrm{L}^2}\right)\right]\right] \tag{33}$$

$$= \frac{\mu\,|b|}{2\pi(1-\nu)}\ell 0.0294\ln\left(\frac{\nabla\rho_{\mathrm{GND}}}{\ell\,\rho_{\mathrm{SSD}}}\right)\ln\left(1+\rho_{\mathrm{GND}}\ell^2\right) \tag{34}$$

$$= \frac{\mu\,|b|}{2\pi(1-\nu)}D''\ln\left(\frac{\nabla\rho_{\mathrm{GND}}}{\ell\,\rho_{\mathrm{SSD}}}\right), \tag{35}$$

where D'' is the associated material parameter, reads

$$D'' = 0.0294\ell\ln\left(1+\rho_{\mathrm{GND}}\ell^2\right). \tag{36}$$

Under the condition $\mathcal{X} \geq 1$, the value of ρ_{GND} and ℓ are way smaller than one, therefore,

$$D'' \approx 0.0588\ell\ln(1) = 0. \tag{37}$$

It should be noted that, in contrast, the back stress formulation derived from the usage of Puiseux's series exhibits a logarithmic dependency on $\frac{\nabla\rho_{\mathrm{GND}}}{\ell\,\rho_{\mathrm{SSD}}}$. Unlike $\tau^{\xi}_{\mathrm{nfc},\mathcal{X}<1}$, the associate material parameter D'' shows a tendency approaching

Table 2
Summary of the nearfield correction stress by different approximation methods for the probability density function.

approximation method	$\tau^{\xi}_{\mathrm{nfc}}$	dependency on $\frac{\nabla\rho_{\mathrm{GND}}}{\rho_{\mathrm{SSD}}}$	associated material parameter
Maclaurin's series	$\tau^{\xi}_{\mathrm{nfc},\mathcal{X}<1} = \frac{\mu\lvert b\rvert}{2\pi(1-\nu)} D' \frac{\nabla\rho_{\mathrm{GND}}}{\rho_{\mathrm{SSD}}}$	linear	$D' = 0.0588\ell\sqrt{\rho_{\mathrm{GND}}}\arctan\left(\ell\sqrt{\rho_{\mathrm{GND}}}\right)$
Puiseux's series	$\tau^{\xi}_{\mathrm{nfc},\mathcal{X}\geq 1} = \frac{\mu\lvert b\rvert}{2\pi(1-\nu)} D'' \ln\left(\frac{\nabla\rho_{\mathrm{GND}}}{\ell\rho_{\mathrm{SSD}}}\right)$	logarithmic	$D'' = 0.0294\ell\ln\left(1+\rho_{\mathrm{GND}}\ell^2\right)$

to zero within the applicable regime (low ρ_{SSD} and ℓ). Therefore, the internal stress, $\tau^{\xi}_{\mathrm{nfc},\mathcal{X}\geq 1}$, is always close to zero under the condition of $\mathcal{X} \geq 1$.

The resulting nearfield correction stress, obtained using different expansion methods, along with the corresponding material parameters used in each derivation, are summarized in Table 2. The nearfield correction stress include two different formulations according to the value of $\mathcal{X}$. Based on the composition of parameters within $\mathcal{X}$, $\mathcal{X}$ can serve as a criterion of the transition between discrete and continuum regimes. In a discrete coarse-graining volume, the value of ρ_{SSD} is small. Consequently, a discrete coarse-graining volume will lead to higher $\mathcal{X}$. Regarding the role of $dist$, it can be represented by the attraction zone adjacent to an edge dislocation wall (as defined in Eq. (11)), which is the smallest value of $dist$. A smaller $dist$ is resulting from a more dilute GND wall, therefore, also a higher value of $\mathcal{X}$. Additionally, considering the numerical discretization level, a smaller element size ℓ corresponds to a higher numerical discontinuity, leading to increased or even divergent gradients across the coarse-graining in numerical calculation. Consequently, a coarse-graining volume with high microstructural and numerical discontinuity results in a high value of $\mathcal{X}$.

6. Discussion

Within Section 6, we first discuss the role of $\mathcal{X}$ in numerical calculation serving as the criterion that indicates the transition between discrete and continuum modeling methods, as well as the behavior and implications of both $\tau^{\xi}_{\mathrm{nfc},\mathcal{X}<1}$ and $\tau^{\xi}_{\mathrm{nfc},\mathcal{X}\geq 1}$. We then look into the influence of different dislocation densities on the heterogeneity, so as to examine the role of ρ_{SSD} within the probability function d and the nearfield correction stress. We further propose a physical interpretation for the material length scale in the work-conjugated gradient plasticity.

6.1. The Transition from Discrete to Continuous

In Section 5, we derived two versions of $\tau^{\xi}_{\mathrm{nfc}}$ based on the range of $\mathcal{X}$. To gain a better understanding of the applicability of different versions of $\tau^{\xi}_{\mathrm{nfc}}$, we look into the physical meaning of $\mathcal{X}$. $\mathcal{X}$ can be interpreted as a physical parameter that reflects the level of continuity within the coarse-graining volume considering both numerical and microstructural aspects. An increase in $\mathcal{X}$ arises from two factors as discussed in the end of Section 5.2:

1. Dislocation diluteness: The low value of ρ_{SSD} in the coarse-graining indicates a scarcity of SSDs. Also, the smallest value of $dist$, which is the attraction zone besides a GND wall, affects the value of $\mathcal{X}$. A more dilute GND wall leads to a smaller attraction zone. Consequently, the increase in $\mathcal{X}$ resulting from the decrease in ρ_{SSD} and $dist$ corresponds to a reduction in the microstructure's continuity within the coarse-graining.
2. Increasing the numerical discretization level, which corresponds to shrinking the element size, results in an intensified degree of discontinuity across the elements. This enhanced discontinuity leads to steep gradients in the calculated state variables, specifically $\nabla\rho_{\mathrm{GND}}$ across the elements in our case. In the context of a coarse-graining method, the steep gradients can limit the resolution and accuracy of the calculations. Therefore, the amplified $\nabla\rho_{\mathrm{GND}}$ resulting from the shrinkage of the coarse-graining volume leads to an increase in the parameter $\mathcal{X}$, indicating a greater level of numerical discontinuity in the coarse-graining approach

The continuous version of nearfield correction stress, which employs the expansion of the probability density function when $\mathcal{X} < 1$, approximates microstructure heterogeneity of a continuous coarse-graining volume. The resulting $\tau^{\xi}_{\mathrm{nfc},\mathcal{X}<1}$ (see the first row in Table 2) exhibits a linear dependence on $\frac{\nabla\rho_{\mathrm{GND}}}{\rho_{\mathrm{SSD}}}$ and bears resemblance to the back stress term within work-conjugated crystal plasticity theories. Regarding the discrete version of nearfield correction stress, $\tau^{\xi}_{\mathrm{nfc},\mathcal{X}\geq 1}$ (see the second row in Table 2), which is calculated by the heterogeneity of a discontinuous coarse-graining volume, displays a logarithmic dependency on $\frac{\nabla\rho_{\mathrm{GND}}}{\ell\rho_{\mathrm{SSD}}}$. Additionally, the associated material parameters of

the two versions of nearfield correction stresses also exhibit very distinguished behaviors. For the continuous version, D' has an arc-tangent relation to element size and the GND density. Therefore, within the continuous regime, as the coarse-graining volume evolves to a discrete condition, i.e., ℓ and ρ_{GND} decreases, the value of D' will also decrease. Such that, D' has a normalization effect to the nearfield correction stress. It can effectively prevent the divergence behavior induced by the scaling characteristics of $\frac{1}{\rho}$, as well as the shrinkage of the element size. On the contrary, D'' has a logarithmic dependency on the value of $\left(1+\rho_{\mathrm{GND}}\ell^2\right)$. Thereby, D'' tends to be zero, since $\rho_{\mathrm{GND}}\ell^2 \ll 1$ within the discrete regime. It can be understood that the inhomogeneity within the coarse-graining volume under a discrete numerical and microstructural condition tends to fluctuate randomly. Thus, the formation of a considerable internal stress field is not possible and can be neglected within continuum models. The homogenization approach also becomes unnecessary. The discrete version of nearfield correction stress, $\tau^{\xi}_{\mathrm{nfc},\mathcal{X}\geq 1}$, is therefore expected to have a value close to zero within the discrete regime.

6.2. A Physical Interpretation for the Material Length Scale

Within the formulation of $\tau^{\xi}_{\mathrm{nfc},\mathcal{X}<1}$ (see the first row in Table 2), which is similar to the backstress term in the continuous crystal plasticity model, ρ_{GND} occurs within the material parameter D', and ρ_{SSD} contributes as a scaling factor toward the heterogeneity distribution aligning with the material length scale within work-conjugated gradient plasticity theories discussed within Section 1. Here, we would like to investigate the role of ρ_{GND} and ρ_{SSD} within the nearfield correction stress, and also conduct a further comparison with the material length scale of back stresses for gradient plasticity theories.

We have shown the influence of different dislocation densities on the distribution of heterogeneity by Fig. 11. In the upper row of Fig. 11, which demonstrates case(1) within Section 5.1, a clear trend is evident: the heterogeneity increases significantly with higher values of ρ_{GND}. The leftmost histogram in the upper row, corresponding to a relatively low value of ρ_{GND} (i.e., $20\mu m^{-2}$), displays a completely random distribution of GND walls. This result indicates that heterogeneity within a coarse-graining volume arises from the presence of excessive dislocations. A substantial quantity of excessive dislocations is necessary for the formation of heterogeneity within coarse-graining volumes. In contrast, the lower row of Fig. 11 presenting the trend of case(2) demonstrates a clear trend towards a more uniform distribution of probability as the value of ρ_{SSD} increases. An increase in ρ_{SSD} leads to a noticeable shift towards more equal probabilities and random distribution of GND walls. This observation indicates reduced heterogeneity caused by the presence of a higher quantity of SSDs.

For better analysis of the impact of ρ_{SSD} on the internal stress, we further investigate the resulting microstructure heterogeneity and stress field under the influence of ρ_{SSD}. In Fig. 12a, the distribution of GND walls appears to be more uniform and scattered. In contrast, Fig. 12b displays a more concentrated and integrated distribution of GND walls. This explains our observations from Fig. 11 that the reducing heterogeneity can be attributed to the presence of SSDs within the coarse-graining volume. If we look into the stress field induced by a dipole structure, the influence of each SSD is short-range. However, each SSD still provides a significant stress field within a very close region as shown in Fig. 3c, which acts as a hindrance and disrupts the movement of the GND walls. As a result, the GND walls in Fig. 12a are fragmented into smaller fractions and exhibit a more random distribution. Thereby, we can infer that although the SSDs do not contribute to the near-field correction stress, they play a crucial role in interacting with the movement of GND walls. The resulting stress fields induced by the microstructures depicted in Fig. 12a and Fig. 12b are plotted in Fig. 12c and Fig. 12d respectively. It is evident that the resulting stress field under the case with higher ρ_{SSD} is lower, with an average value of 468 MPa, and exhibits a more non-uniform distribution. On the other hand, the case with lower ρ_{SSD} yields a higher stress field with an average value of 757 MPa that is more uniformly distributed throughout the coarse-graining volume. It is expected that a higher level of heterogeneity leads to higher internal stress.

In conclusion, the inclusion of ρ_{SSD} in the derivation of the nearfield correction stress is crucial for influencing the formation of heterogeneity within the coarse-graining volume. It represents the quantity of obstacles that impede the development and movement of microstructure heterogeneity. By comparing the derivation of the nearfield correction stress to the back stress term in work-conjugated gradient plasticity theory, we can provide a physical explanation for the material length scale. This length scale can be interpreted as the average spacing within the coarse-graining volume at which a GND wall encounters an SSD. It effectively measures the distance a GND wall can travel without being hindered or broken by SSDs. Therefore, a larger material length scale indicates a higher level of heterogeneity that needs to be considered within the coarse-graining volume. Therefore, the scaling effect by ρ_{SSD} can be understood as the factor deciding the heterogeneity level within a coarse-graining volume. If we replace ρ_{SSD} within Eq. (18) by

ρ_{GND} as the material length scale, a low value of ρ_{GND} results in a large internal stress. This formulation does not meet the observations from Fig. 11 and Fig. 12, as well as our assumption that the existence of the nearfield stress term is meant to resolve the internal stress induced by the heterogeneity within a coarse-graining. Moreover, it also implies a system without any strain gradient would have an infinite magnitude of back stress and cause instability as discussed within the publications of Bardella and Panteghini (2015); Wulfinghoff and Böhlke (2015); Wulfinghoff et al. (2015). Regarding the influence of ρ_{GND} on the magnitude of $\tau^{\xi}_{\mathrm{nfc},\mathcal{X}<1}$, it is considered by the value of D'. A large amount of excessive dislocations results in a higher value of D' so as $\tau^{\xi}_{\mathrm{nfc},\mathcal{X}<1}$. And as the value of ρ_{GND} is close to zero, the value of D' as well as $\tau^{\xi}_{\mathrm{nfc},\mathcal{X}<1}$ will tend to be zero since the presence of excessive dislocations is essential for the formation of heterogeneity within coarse-graining volumes as we observed from the upper row within Fig. 11. To be noted, the material parameter D' associated with $\tau^{\xi}_{\mathrm{nfc},\mathcal{X}<1}$ is a function dependent on numerical length scale ℓ and the average spacing between excessive dislocations $\sqrt{\rho_{\mathrm{GND}}}$. The determination of this value within the back stress term has also been a long-lasting issue within both dislocation-based crystal plasticity theories (e.g., Yefimov et al. (2004); Kuroda and Needleman (2019)) and statistical theories (e.g., Groma et al. (2003); Ispánovity et al. (2020)). The data-based homogenization approach from discrete to continuum regime physically introduced different dislocation densities (material length scales) into the nearfield correction stress automatically. It avoids the difficulties of determining material parameters while implemented into the numerical framework. Also, it is derived for a highly flexible numerical discretization scheme based on both the microstructure and numerical length scales of the coarse-graining volume.

7. Conclusion

We introduced a homogenization method addressing heterogeneity at the numerical length scale for continuous crystal plasticity theories. Using DDD simulations, we simulated microstructure heterogeneity within an element, taking into account the influence of neighboring averaging elements. Our analysis shows that heterogeneity within a coarse-graining volume in continuous crystal plasticity methods comprises randomly distributed SSDs and non-uniformly distributed GND walls. The SSDs do not contribute to any long-range stress field. Conversely, the GND walls result in the emergence of noticeable stress fields within the coarse-graining volume.

Based on these findings, we propose a homogenization approach to calculate the nearfield correction stress field, $\tau^{\xi}_{\mathrm{nfc}}$, induced by the heterogeneity within the coarse-graining volume. $\tau^{\xi}_{\mathrm{nfc}}$ is calculated by the convolution between the GND wall density function and the stress field generated by a single GND wall. The GND wall density function is derived through a data-based approach. The dataset was obtained from a large amount of DDD simulations. We conducted simulations to compute different GND wall distributions within coarse-graining volume under various combinations of state variables.

The direct homogenization from discrete to continuum formulation as presented in this study physically addresses microstructure heterogeneity within the coarse-graining. We derived two versions of the nearfield correction stress based on the range of $\mathcal{X}$. The continuous version of nearfield correction stress $\tau^{\xi}_{\mathrm{b},\mathcal{X}<1}$ has a similar formulation of the classical back stress term within the work-conjugated gradient plasticity theories. The associated material parameter D' is dependent on the microstructure and numerical parameters and has a normalization effect to prevent the divergent behavior as the coarse-graining volume evolves to the discrete regime. The discrete version of nearfield correction stress, $\tau^{\xi}_{\mathrm{nfc},\mathcal{X}\geq 1}$, corresponding to a coarse-graining volume under discrete microstructure and numerical condition. The associated material parameter D'' has the tendency approaching to zero within the discrete regime, which indicates that within a discrete regime, the nearfield correction stress is negligible. $\mathcal{X}$ is therefore the criterion indicating the transition between the discrete and continuum regime in a numerical dislocation-based continuum approach that comes with strongly flexible discretization schemes.

Upon examining the derivation of the nearfield correction stress and analyzing the DDD dataset, we have found that the presence of SSDs as obstacles impede the movement of GND walls, leading to a noticeable decrease in heterogeneity within the coarse-graining volume. As a result, an increase in the value of ρ_{SSD} corresponds to reduced heterogeneity. Therefore, for $\tau^{\xi}_{\mathrm{b},\mathcal{X}<1}$, which is scaled by the inverse of ρ_{SSD}, the material length scale can be understood as the average spacing for a GND wall encounter obstacles (SSDs). This finding offers a physical explanation for the material length scale within the work-conjugated gradient plasticity theories.

Data availability

Data will be made available on request.

Acknowledgment

The financial support of this work in the context of the German Research Foundation (DFG) project SCHU 3074/3-1 is gratefully acknowledged. The simulation work was performed on the computational resource HoreKa funded by the Ministry of Science, Research and the Arts Baden-Württemberg and DFG, Germany.

References

Aifantis, E.C., 1984. On the microstructural origin of certain inelastic models. Journal of Engineering Materials and Technology 106, 326–330.

Albiez, J., Erdle, H., Weygand, D., Böhlke, T., 2019. A gradient plasticity creep model accounting for slip transfer/activation at interfaces evaluated for the intermetallic nial-9mo. International Journal of Plasticity 113, 291–311.

Amodeo, R.J., Ghoniem, N.M., 1990. Dislocation dynamics. i. a proposed methodology for deformation micromechanics. Physical Review B 41, 6958.

Arsenlis, A., Cai, W., Tang, M., Rhee, M., Oppelstrup, T., Hommes, G., Pierce, T.G., Bulatov, V.V., 2007. Enabling strain hardening simulations with dislocation dynamics. Modelling and Simulation in Materials Science and Engineering 15, 553.

Arsenlis, A., Parks, D., 1999. Crystallographic aspects of geometrically-necessary and statistically-stored dislocation density. Acta materialia 47, 1597–1611.

Bardella, L., Panteghini, A., 2015. Modelling the torsion of thin metal wires by distortion gradient plasticity. Journal of the Mechanics and Physics of Solids 78, 467–492.

Berdichevsky, V., 2006. On thermodynamics of crystal plasticity. Scripta materialia 54, 711–716.

Berdichevsky, V., Dimiduk, D., 2005. On failure of continuum plasticity theories on small scales. Scripta materialia 52, 1017–1019.

Bhattacharyya, J., Bittmann, B., Agnew, S., 2019. The effect of precipitate-induced backstresses on plastic anisotropy: Demonstrated by modeling the behavior of aluminum alloy, 7085. International Journal of Plasticity 117, 3–20.

Chollet, F., et al., 2015. Keras. https://keras.io.

Chong, A., Yang, F., Lam, D.C., Tong, P., 2001. Torsion and bending of micron-scaled structures. Journal of Materials Research 16, 1052–1058.

Cui, Y., Liu, Z., Zhuang, Z., 2015. Quantitative investigations on dislocation based discrete-continuous model of crystal plasticity at submicron scale. International Journal of Plasticity 69, 54–72.

Date, E., Andrews, K., 1969. Anisotropic and composition effects in the elastic properties of polycrystalline metals. Journal of Physics D: Applied Physics 2, 1373.

Davey, W.P., 1925. Precision measurements of the lattice constants of twelve common metals. Physical Review 25, 753.

Dogge, M.M., Peerlings, R.H., Geers, M.G., 2015. Extended modelling of dislocation transport-formulation and finite element implementation. Advanced Modeling and Simulation in Engineering Sciences 2, 1–18.

Evers, L., Parks, D., Brekelmans, W., Geers, M., 2002. Crystal plasticity model with enhanced hardening by geometrically necessary dislocation accumulation. Journal of the Mechanics and Physics of Solids 50, 2403–2424.

Fleck, N., Muller, G., Ashby, M.F., Hutchinson, J.W., 1994. Strain gradient plasticity: theory and experiment. Acta Metallurgica et materialia 42, 475–487.

Forest, S., 2019. Micromorphic approach to gradient plasticity and damage. Handbook of Nonlocal Continuum Mechanics for Materials and Structures , 499–546.

Geers, M., Brekelmans, W., Bayley, C., 2006. Second-order crystal plasticity: internal stress effects and cyclic loading. Modelling and Simulation in Materials Science and Engineering 15, S133.

Geers, M., Cottura, M., Appolaire, B., Busso, E.P., Forest, S., Villani, A., 2014. Coupled glide-climb diffusion-enhanced crystal plasticity. Journal of the Mechanics and Physics of Solids 70, 136–153.

Geers, M., Peerlings, R., Peletier, M., Scardia, L., 2013. Asymptotic behaviour of a pile-up of infinite walls of edge dislocations. Archive for Rational Mechanics and Analysis 209, 495–539.

Van der Giessen, E., Needleman, A., 1995. Discrete dislocation plasticity: a simple planar model. Modelling and Simulation in Materials Science and Engineering 3, 689.

Groma, I., Csikor, F., Zaiser, M., 2003. Spatial correlations and higher-order gradient terms in a continuum description of dislocation dynamics. Acta Materialia 51, 1271–1281.

Groma, I., Györgyi, G., Kocsis, B., 2007. Dynamics of coarse grained dislocation densities from an effective free energy. Philosophical Magazine 87, 1185–1199.

Groma, I., Zaiser, M., Ispánovity, P.D., 2016. Dislocation patterning in a two-dimensional continuum theory of dislocations. Physical Review B 93, 214110.

Guo, S., He, Y., Lei, J., Li, Z., Liu, D., 2017. Individual strain gradient effect on torsional strength of electropolished microscale copper wires. Scripta Materialia 130, 124–127.

Gurtin, M.E., 2000. On the plasticity of single crystals: free energy, microforces, plastic-strain gradients. Journal of the Mechanics and Physics of Solids 48, 989–1036.

Gurtin, M.E., 2002. A gradient theory of single-crystal viscoplasticity that accounts for geometrically necessary dislocations. Journal of the Mechanics and Physics of Solids 50, 5–32.

Gurtin, M.E., Anand, L., Lele, S.P., 2007. Gradient single-crystal plasticity with free energy dependent on dislocation densities. Journal of the Mechanics and Physics of Solids 55, 1853–1878.
Gurtin, M.E., Ohno, N., 2011. A gradient theory of small-deformation, single-crystal plasticity that accounts for gnd-induced interactions between slip systems. Journal of the Mechanics and Physics of Solids 59, 320–343.
Hirth, J.P., Lothe, J., 1982. Theory of dislocations. Wiley, New York.
Hochrainer, T., 2016. Thermodynamically consistent continuum dislocation dynamics. Journal of the Mechanics and Physics of Solids 88, 12–22.
Hochrainer, T., Sandfeld, S., Zaiser, M., Gumbsch, P., 2014. Continuum dislocation dynamics: towards a physical theory of crystal plasticity. Journal of the Mechanics and Physics of Solids 63, 167–178.
Hussein, A.M., Rao, S.I., Uchic, M.D., Dimiduk, D.M., El-Awady, J.A., 2015. Microstructurally based cross-slip mechanisms and their effects on dislocation microstructure evolution in fcc crystals. Acta Materialia 85, 180–190.
Ispánovity, P.D., Groma, I., Györgyi, G., 2008. Evolution of the correlation functions in two-dimensional dislocation systems. Physical Review B 78, 024119.
Ispánovity, P.D., Papanikolaou, S., Groma, I., 2020. Emergence and role of dipolar dislocation patterns in discrete and continuum formulations of plasticity. Physical Review B 101, 024105.
Izadbakhsh, A., Inal, K., Mishra, R.K., Niewczas, M., 2011. New crystal plasticity constitutive model for large strain deformation in single crystals of magnesium. Computational materials science 50, 2185–2202.
Jafari, M., Jamshidian, M., Ziaei-Rad, S., Raabe, D., Roters, F., 2017. Constitutive modeling of strain induced grain boundary migration via coupling crystal plasticity and phase-field methods. International Journal of Plasticity 99, 19–42.
Jebahi, M., Cai, L., Abed-Meraim, F., 2020. Strain gradient crystal plasticity model based on generalized non-quadratic defect energy and uncoupled dissipation. International Journal of Plasticity 126, 102617.
Jiang, J., Britton, T., Wilkinson, A., 2013. Evolution of dislocation density distributions in copper during tensile deformation. Acta Materialia 61, 7227–7239.
Keralavarma, S., Curtin, W., 2016. Strain hardening in 2d discrete dislocation dynamics simulations: a new '2.5 d'algorithm. Journal of the Mechanics and Physics of Solids 95, 132–146.
Kubin, L.P., Canova, G., Condat, M., Devincre, B., Pontikis, V., Bréchet, Y., 1992. Dislocation microstructures and plastic flow: a 3d simulation, in: Solid state phenomena, Trans Tech Publ. pp. 455–472.
Kuroda, M., Needleman, A., 2019. Nonuniform and localized deformation in single crystals under dynamic tensile loading. Journal of the Mechanics and Physics of Solids 125, 347–359.
Kuykendall, W.P., Cai, W., 2013. Conditional convergence in two-dimensional dislocation dynamics. Modelling and Simulation in Materials Science and Engineering 21, 055003.
Lemarchand, C., Devincre, B., Kubin, L., 2001. Homogenization method for a discrete-continuum simulation of dislocation dynamics. Journal of the Mechanics and Physics of Solids 49, 1969–1982.
Li, J.C., 1960. Some elastic properties of an edge dislocation wall. Acta metallurgica 8, 563–574.
Li, Y.L., Kohar, C.P., Muhammad, W., Inal, K., 2022. Precipitation kinetics and crystal plasticity modeling of artificially aged aa6061. International Journal of Plasticity 152, 103241.
Lin, P., El-Azab, A., 2020. Implementation of annihilation and junction reactions in vector density-based continuum dislocation dynamics. Modelling and Simulation in Materials Science and Engineering 28, 045003.
Ma, A., Roters, F., Raabe, D., 2006. A dislocation density based constitutive model for crystal plasticity fem including geometrically necessary dislocations. Acta Materialia 54, 2169–2179.
Motz, C., Weygand, D., Senger, J., Gumbsch, P., 2009. Initial dislocation structures in 3-d discrete dislocation dynamics and their influence on microscale plasticity. Acta Materialia 57, 1744–1754.
Norfleet, D., Dimiduk, D., Polasik, S., Uchic, M., Mills, M., 2008. Dislocation structures and their relationship to strength in deformed nickel microcrystals. Acta Materialia 56, 2988–3001.
Piao, Y., Le, K.C., 2022. Thermodynamic theory of dislocation/grain boundary interaction. Continuum Mechanics and Thermodynamics 34, 763–780.
Roters, F., Eisenlohr, P., Hantcherli, L., Tjahjanto, D.D., Bieler, T.R., Raabe, D., 2010. Overview of constitutive laws, kinematics, homogenization and multiscale methods in crystal plasticity finite-element modeling: Theory, experiments, applications. Acta materialia 58, 1152–1211.
Roy, A., Peerlings, R., Geers, M., Kasyanyuk, Y., 2008. Continuum modeling of dislocation interactions: why discreteness matters? Materials Science and Engineering: A 486, 653–661.
Ryś, M., Forest, S., Petryk, H., 2020. A micromorphic crystal plasticity model with the gradient-enhanced incremental hardening law. International Journal of Plasticity 128, 102655.
Ryś, M., Petryk, H., 2018. Gradient crystal plasticity models with a natural length scale in the hardening law. International Journal of Plasticity 111, 168–187.
Sandfeld, S., Monavari, M., Zaiser, M., 2013. From systems of discrete dislocations to a continuous field description: stresses and averaging aspects. Modelling and Simulation in Materials Science and Engineering 21, 085006.
Schmitt, S., Gumbsch, P., Schulz, K., 2015. Internal stresses in a homogenized representation of dislocation microstructures. Journal of the Mechanics and Physics of Solids 84, 528–544.
Schulz, K., Dickel, D., Schmitt, S., Sandfeld, S., Weygand, D., Gumbsch, P., 2014. Analysis of dislocation pile-ups using a dislocation-based continuum theory. Modelling and Simulation in Materials Science and Engineering 22, 025008.
Schulz, K., Wagner, L., Wieners, C., 2019. A mesoscale continuum approach of dislocation dynamics and the approximation by a runge-kutta discontinuous galerkin method. International Journal of Plasticity 120, 248–261.
Sills, R.B., Bertin, N., Aghaei, A., Cai, W., 2018. Dislocation networks and the microstructural origin of strain hardening. Physical review letters 121, 085501.

Sudmanns, M., Stricker, M., Weygand, D., Hochrainer, T., Schulz, K., 2019. Dislocation multiplication by cross-slip and glissile reaction in a dislocation based continuum formulation of crystal plasticity. Journal of the Mechanics and Physics of Solids 132, 103695.
Tagarielli, V., Fleck, N., 2011. The shear response of a thin aluminum layer. Journal of Applied Mechanics 78.
Vivekanandan, V., Anglin, B., El-Azab, A., 2023. A data driven approach for cross-slip modelling in continuum dislocation dynamics. International Journal of Plasticity 164, 103597.
Voyiadjis, G.Z., Song, Y., 2019. Strain gradient continuum plasticity theories: theoretical, numerical and experimental investigations. International Journal of Plasticity 121, 21–75.
Weygand, D., Poignant, M., Gumbsch, P., Kraft, O., 2008. Three-dimensional dislocation dynamics simulation of the influence of sample size on the stress–strain behavior of fcc single-crystalline pillars. Materials Science and Engineering: A 483, 188–190.
Wulfinghoff, S., Bayerschen, E., Böhlke, T., 2013. A gradient plasticity grain boundary yield theory. International Journal of Plasticity 51, 33–46.
Wulfinghoff, S., Böhlke, T., 2015. Gradient crystal plasticity including dislocation-based work-hardening and dislocation transport. International Journal of Plasticity 69, 152–169.
Wulfinghoff, S., Forest, S., Böhlke, T., 2015. Strain gradient plasticity modeling of the cyclic behavior of laminate microstructures. Journal of the Mechanics and Physics of Solids 79, 1–20.
Yefimov, S., Groma, I., Van der Giessen, E., 2004. A comparison of a statistical-mechanics based plasticity model with discrete dislocation plasticity calculations. Journal of the Mechanics and Physics of Solids 52, 279–300.
Zaiser, M., 2015. Local density approximation for the energy functional of three-dimensional dislocation systems. Physical Review B 92, 174120.
Zbib, H.M., Rhee, M., Hirth, J.P., 1998. On plastic deformation and the dynamics of 3d dislocations. International Journal of Mechanical Sciences 40, 113–127.
Zhang, X., Lu, S., Zhang, B., Tian, X., Kan, Q., Kang, G., 2021. Dislocation–grain boundary interaction-based discrete dislocation dynamics modeling and its application to bicrystals with different misorientations. Acta Materialia 202, 88–98.
Zhou, C., Biner, S.B., LeSar, R., 2010. Discrete dislocation dynamics simulations of plasticity at small scales. Acta Materialia 58, 1565–1577.